Antigen Recognition Is Facilitated by Invadosome-like Protrusions Formed by Memory/Effector T Cells

Peter T. Sage, Laya M. Varghese, Roberta Martinelli, Tracey E. Sciuto, Masataka Kamei, Ann M. Dvorak, Timothy A. Springer, Arlene H. Sharpe and Christopher V. Carman

J Immunol 2012;188;3686-3699; Prepublished online 21 March 2012;
doi:10.4049/jimmunol.1102594
http://www.jimmunol.org/content/188/8/3686

The Journal of Immunology is published twice each month by The American Association of Immunologists, Inc., 9650 Rockville Pike, Bethesda, MD 20814-3994.

Print ISSN: 0022-1767 Online ISSN: 1550-6606.

Antigen Recognition Is Facilitated by Invadosome-like Protrusions Formed by Memory/Effector T Cells

Peter T. Sage,*,† Laya M. Varghese,† Roberta Martinelli,† Tracey E. Sciuto,‡ Masataka Kamei,† Ann M. Dvorak,‡ Timothy A. Springer,§ Arlene H. Sharpe,* and Christopher V. Carman†

Adaptive immunity requires that T cells efficiently scan diverse cell surfaces to identify cognate Ag. However, the basic cellular mechanisms remain unclear. In this study, we investigated this process using vascular endothelial cells, APCs that possess a unique and extremely advantageous, planar morphology. High-resolution imaging revealed that CD4 memory/effector T cells dynamically probe the endothelium by extending submicron-scale, actin-rich "invadosome/podosome-like protrusions" (ILPs). The intimate intercellular contacts enforced by ILPs consistently preceded and supported T cell activation in response to endothelial MHC class II/Ag. The resulting calcium flux stabilized dense arrays of ILPs (each enriched in TCR, protein kinase C-θ, ZAP70, phosphotyrosine, and HS1), forming what we term a podo-synapse. Similar findings were made using CD8 CTLs on endothelium. Furthermore, careful re-examination of both traditional APC models and professional APCs suggests broad relevance for ILPs in facilitating Ag recognition. Together, our results indicate that ILPs function as sensory organelles that serve as actuators of immune surveillance. ***The Journal of Immunology*****, 2012, 188: 3686–3699.**

Adaptive immunity relies on the ability of TCRs expressed on lymphocytes to efficiently recognize peptide Ag bound to MHC molecules (1). During the priming phase, naive lymphocytes must constitutively scan professional APCs within lymph nodes. During the effector phase, memory/effector T cells need to effectively survey an extremely wide range of APCs and potential target cells within peripheral tissues. Fundamental cellular mechanisms for such immune surveillance activities remain incompletely understood.

At the heart of immune surveillance is the requirement for T cells to form extremely intimate (~14 nm, the total height of the TCR–MHC complex) (2) contacts with apposing cells to sample MHC/Ag. However, the surfaces of all cells are modified by a relatively thick (50–500 nm) gel-like polysaccharide coat termed the glycocalyx (3), which provides a formidable energy barrier (via steric and electrostatic repulsion) to close membrane–membrane encounter (4, 5). In this way, TCR and MHC are effectively shielded and immune recognition is opposed (5–10). Thus, a fundamental question is, how do T cells overcome this energy barrier to engage immune receptors?

It has long been appreciated that as a consequence of Ag recognition, specialized cell–cell interfaces form that involve membrane alignment, cytoskeletal remodeling, clustering/segregation of immune receptors/adhesion molecules, and glycocalyx components (5, 11–15). These "immunological synapses" (ISs) form within minutes of Ag recognition and are thought to amplify and sustain signaling, as well as facilitate exchange of cytokine and/or cytotoxic materials (5, 11–15). However, detailed mechanisms facilitating initial Ag sampling between T cells and APCs, and how these lead to early IS formation, are not completely understood (16, 17). This stems from technical challenges associated with irregular topologies of APC surfaces and poorly controlled orientation of the cell–cell interaction planes, issues that profoundly limit the requisite imaging approaches (16–18).

Investigators have partially circumvented these restrictions by developing planar substrate models (i.e., lipid bilayers and Ab-coated surfaces) that provide optimal spatiotemporal resolution for monitoring Ag response dynamics (19–23). These models have afforded invaluable insights, such as the discovery of TCR microclusters as critical mediators of effective signaling (15, 19–22). However, these systems lack key features of cellular APC surfaces, such as the glycocalyx, topological deformability, and molecular complexity. Therefore, it remains uncertain how to translate such findings to physiologic cell–cell immune surveillance.

In this study, we used vascular endothelial cells (ECs) as a planar APC model to interrogate the details of initial Ag recognition dynamics on a physiologic cellular substrate. ECs represent the interface between the blood circulation and tissue, and play critical roles in regulating immune cell trafficking (1, 24, 25). The dis-

*Department of Microbiology and Immunobiology, Harvard Medical School, Boston, MA 02115 †Department of Medicine, Center for Vascular Biology Research, Beth Israel Deaconess Medical Center, Harvard Medical School, Boston, MA 02215; ‡Department of Pathology, Center for Vascular Biology Research, Beth Israel Deaconess Medical Center, Harvard Medical School, Boston, MA 02215; and §Department of Pathology, Immune Disease Institute, Harvard Medical School, Boston, MA 02115

Received for publication September 14, 2011. Accepted for publication February 13, 2012.

This work was supported by the National Institutes of Health (Grants T32 AI070085 to P.T.S., AI078897 to A.H.S., and HL04006 to C.V.C.) and the American Heart Association, the Arthritis Foundation, and the Roche Organ Transplant Research Foundation (to C.V.C.).

Address correspondence and reprint requests to Christopher V. Carman, Harvard Medical School—Beth Israel Deaconess Medical Center, 330 Brookline Avenue, RN234, Boston, MA 02215. E-mail address: ccarman@bidmc.harvard.edu

The online version of this article contains supplemental material.

Abbreviations used in this article: BMDC, bone marrow-derived dendritic cell; CAMKII, calcium-calmodulin–dependent kinase II; CHO, Chinese hamster ovary; DC, dendritic cell; EC, endothelial cell; HDMVEC, human dermal microvascular EC; HLMVEC, human lung microvascular EC; HS1, hematopoietic lineage cell-specific protein 1; HUVEC, human umbilical vein EC; ILP, invadosome/podosome-like protrusion; IRM, interference reflection microscopy; IS, immunological synapse; iT_{mem}, induced/expanded human T memory cell; mem-DsRed, palmitoylated DsRed; mem-YFP, palmitoylated YFP; MHC-I, MHC class I; MHC-II, MHC class II; nT_{mem}, natural human T memory cell; PKC, protein kinase C; SA, streptavidin; SEB, staphylococcal enterotoxin B; TSST, toxic shock syndrome toxin 1.

covery that ECs express MHC class I (MHC-I), MHC class II (MHC-II), and a large number of costimulatory molecules (e.g., CD40, LFA-3, ICOSL, 4-1BB, OX40L, TL1A, PD-L1, but not CD80 and CD86) has led to the controversial hypothesis that endothelium can also function as a type of APC (26–28). Indeed, several studies have demonstrated that endothelium can effectively restimulate CD4 and CD8 memory/effector, but not naive, T cells (29–33). Critically, when grown in vitro, ECs form virtually planar cell surfaces that are ideal for high spatiotemporal resolution imaging of topological dynamics (34).

This study provides a detailed investigation of the initial events in CD4 and CD8 T cell scanning for Ag. We previously discovered that lymphocytes actively probe the surface of the endothelium by dynamic insertion and retraction of submicron-scale, actin-rich cylindrical protrusions related to invadosomes (35), termed invadosome/podosome-like protrusions (ILPs) (34). These were demonstrated to function in supporting migratory pathfinding (34, 36). In this study, we found that dynamic ILP probing by CD4 and CD8 memory/effector lymphocytes enforces close T cell–EC apposition, which seems to facilitate Ag recognition and TCR signaling. Moreover, T cell activation is sustained through a novel IS architecture dominated by dense arrays of calcium-stabilized ILPs (each enriched in signaling molecules) that we term a podosynapse. Complementary studies with model substrates and professional APCs (B cells and dendritic cells [DCs]) suggest that rather than being a unique feature of T cell–EC ISs, ILPs are uniquely revealed in this setting. Together, our results indicate that memory/effector T cells use ILPs to facilitate efficient search for Ag and to help sustain the resulting signaling responses.

Materials and Methods

Cells

Natural human T memory cells (nT_{mem}; $CD4^+CD45RO^+CD45RA^-$) were isolated via negative selection from peripheral blood using a CD4 T cell isolation kit, followed by $CD45RA^+$ cell depletion (Miltenyi Biotec) to >95% purity. Induced/expanded human T memory cells (iT_{mem}; $CD4^+CD45RO^+$) were made by culturing peripheral blood buffy coats for 72 h in 1 μg/ml bacterial superantigens staphylococcal enterotoxin B (SEB) and toxic shock syndrome toxin 1 (TSST; Toxin Technology). CD4 memory cells were enriched by using a CD4 T cell memory negative isolation kit (Miltenyi Biotec). Cells were cultured 3–10 d in 20 ng/ml IL-15 (R&D Systems) to maintain memory phenotype. Mouse CD4 or CD8 T cells were isolated by magnetic separation from either $OTII^+TCR\alpha^{-/-}CD45.1^{+/+}$ or $OTI^+Thy1.1^{+/+}$ mice and activated with irradiated splenocytes in the presence of 30 μg/ml OVA 323–339 (OTII) or 500 ng/ml OVA-SIINFEKL (OTI) supplemented with IL-2 for 3 d. T cells were reselected with MACS beads and rested in culture in the presence of IL-2 for a further 3 d. Human lung microvascular ECs (HLMVECs), human dermal microvascular ECs (HDMVECs), and human umbilical vein ECs (HUVECs) were from Lonza and cultured on fibronectin (10 μg/ml; Invitrogen) in EBM-2 MV media (Lonza). Mouse heart ECs were isolated from C57BL/6 mice by collagenization of heart tissue followed by positive selection with anti-CD31 (MEC13.3)–coated beads (Invitrogen). ECs were cultured for 7 d in media with EC growth supplement (Biomedical Technologies) followed by reselection with beads coupled to anti-CD102. ECs were >95% purity based on expression of $CD105^+CD102^+$. ECs were transfected by Amaxa electroporation according to manufacturer's instructions (Lonza). Palmitoylated YFP (mem-YFP) and soluble monomeric DsRed were from Clontech. Palmitoylated DsRed (mem-DsRed) and ICAM-1–GFP were generated as described previously (34). ECs were activated for 48 h with 100 ng/ml IFN-γ (R&D Systems) and 12 h with 50 ng/ml TNF-α (R&D Systems). Priess B cell line was a gift from Dr. Kai Wucherpfennig. Chinese hamster ovary (CHO)-K1 epithelial cells were from American Type Culture Collection. Murine bone marrow-derived DCs (BMDCs) were prepared from bone marrow cells cultured in 30 ng/ml GM-CSF (PeproTech) for 6 d.

Transendothelial migration

Lymphocyte transendothelial migration assays were conducted in both static and shear conditions as described previously (34). In some cases, T cells were added to 8-μm pore transwell inserts that were preceded with ECs and then collected from the bottom chamber 6 h later and analyzed by flow cytometry.

Live-cell imaging and analysis

Live-cell imaging was performed on an Axiovert S200 microscope with Axiovision software (Zeiss). For calcium imaging, T cells were preincubated with 1 μg/ml Fura-2–AM or Fluo-4–AM (Invitrogen) for 30 min. For Fura-2, standard Fura-2 filters were used according to manufacturer's instructions (Chroma) and ratiometric calcium flux was calculated (340_{nm}EX-510_{nm}EM-background/380_{nm}EX-510_{nm}EM-background) for each cell using Axiovision. For Fluo-4, green fluorescence filters were used and basal fluorescence signal was established by imaging cells on uncoated chambers. T cell polarity was calculated from bright-field images as the ratio of the greatest edge-to-edge dimension in the *x–y* plane (i.e., the long axis) divided by the perpendicular axis. Migration velocity was measured for cells using the Axiovision Cell Tracking Module. Podo-print/ILP lifetimes were assessed using podo-print appearance and disappearance on mem-dsRed– or mem-YFP–transfected ECs as a readout for the presence of ILPs (34). Podo-print/ILP lifetimes were calculated as follows: the last time point when an individual podo-print/ILP was visible − the time point when that podo-print/ILP first appeared. Podo-print/ILP lateral translocation was assessed by determining the distance between the T cell centroid and the first and last positions of an individual podo-print/ILP during its lifetime. Podo-print/ILP index, a measure of the total number of ILPs per cell, was calculated at 5 min after addition of T cells. "Offset time" was used to describe relative time between first podo-print/ILP formation and calcium flux rise above background. Temporal resolution was limited to 10 s, the maximal achievable acquisition frame rate of this analysis. Data was then sorted into 10-s interval bins.

For selected studies, lymphocytes were preincubated, or lymphocyte and APCs coincubated, with select pharmaceutical agents, including latrunculin A (1 μg/ml; Sigma), BAPTA-AM (40 μM, Sigma), BTP2 (20 μM; Calbiochem), thapsigargin (1 μM Sigma), and calcium-calmodulin–dependent kinase II (CAMKII) inhibitor CK59 (50 μM; EMD Biosciences) as indicated. For calcium blockade conditions, T cells were pretreated with BAPTA-AM and BTP2 in imaging buffer containing high (45 mM) potassium. T cells were added to ECs and imaged with additional BTP2 for the duration of imaging.

Fixed cell imaging

Fixed cell samples were imaged on an LSM 510 confocal microscope (Zeiss). Samples were fixed and stained for αL integrin (TS2/4), ICAM-1 (IC1/11), F-actin (phalloidin), MHC-II (WR18; Abcam), protein kinase C (PKC)-θ, talin (rabbit anti-talin, a gift from Dr. Keith Burridge), CD3 (OKT3; eBioscience), CD43 (L60; BD Biosciences), CD45 (HI30 or UCHL1; eBioscience), hematopoietic lineage cell-specific protein 1 (HS1; clone 9 [BD Biosciences] or rabbit anti-HS1 [Cell Signaling]), ZAP70 (Santa Cruz), phosphotyrosine (4G10 platinum; Millipore), or NFAT (BD Biosciences). Transmigration was analyzed by confocal microscopy as described previously (37).

CTL killing assay

For specific killing assay, murine ECs were labeled with either 0.6 or 0.02 μM CFSE ($CFSE^{hi}$ and $CFSE^{low}$, respectively). The $CFSE^{hi}$ population was pulsed with 1 μg/ml SIINFEKL for 20 min. Both $CFSE^{hi}$ and $CFSE^{low}$ populations were plated together in a 1:1 ratio. Activated OTI CD8 T cells were rested for 5 h and added to monolayers in a 3:1 T cell/target cell ratio. Cultures were stained for CD105 to differentiate the ECs from T cells and analyzed by flow cytometry. Specific lysis was calculated by the following equation: $1 - ([CFSE^{hi}]/([CFSE^{hi} + CFSE^{low}])/[\text{control } CFSE^{hi}/CFSE^{low}])*100$.

Planar coated-glass APC model

Coated glass IS models were prepared as described previously (20, 38). In brief, imaging chambers were coated with ICAM-1–Fc (10 μg/ml; R&D Systems) alone or together with anti-CD3, anti-CD43, anti-CD45, or control IgG Ab (10 μg/ml). Fluo-4–labeled lymphocytes were added and imaged by fluorescence and interference reflection microscopy (IRM).

Coated cell APC model

CHO-K1 cells were transfected with ICAM-1-GFP and soluble dsRed via electroporation. Cells were then coated with Abs via a biotin/streptavidin (SA)-based approach (39). Cells were subjected to primary amine-targeted

cell surface biotinylation for 15 min with biotin-NHS-ester (0.5 μg/ml; Thermo Electron). Cells were incubated with SA at 10 μg/ml for 15 min. Cells were then incubated with biotinylated anti-CD3, -CD43, or -CD45 (eBioscience) at 10 μg/ml for 15 min.

T cell activation by CD3 cross-linking

Fluo-4–labeled T cells were settled onto uncoated glass chambers, 10 μg/ml anti-CD3 and -CD28 were added to the imaging chambers, and calcium was monitored.

Transmission electron microscopy

Transmission electron microscopy of T cell–APC complexes was performed as described previously (34). Fifty randomly selected micrographs were analyzed by enumerating zones of membrane apposition (<20 nm) and correlating them with respect to ILP location.

Statistical analysis

Error bars represent SE or SD as indicated. The p values were calculated via unpaired Student t tests in GraphPad Prism. Statistical significance is indicated with p values as follows: $***p < 0.0005$, $**p < 0.005$, $*p < 0.05$.

Results

Endothelial-presented Ag promotes activation of CD4 memory T cells

We wanted to elucidate the mechanisms by which memory/effector T cells probe for Ag using ECs as model APCs. Therefore, we isolated natural CD4 memory-like lymphocytes (nT_{mem}) and generated induced/expanded CD4 memory-like lymphocytes (iT_{mem}) from human peripheral blood. The isolated nT_{mem} were $CD4^+$, $CD45RO^+$, and contained both central memory and effector memory T cells (~78 and ~22%, respectively) based on CD62L staining (Supplemental Fig. 1A). The iT_{mem} were slightly more polarized toward the effector memory T cell subtype (~69 versus ~31%; Supplemental Fig. 1B). Monolayers of HLMVECs, HDMVECs, and HUVECs were used as models for the vasculature. In vivo endothelial MHC-II expression is dependent on IFN-γ (26). This was recapitulated in vitro by culturing ECs with exogenous IFN-γ (Supplemental Fig. 1C). Endothelium was additionally activated with TNF-α to promote an inflamed phenotype.

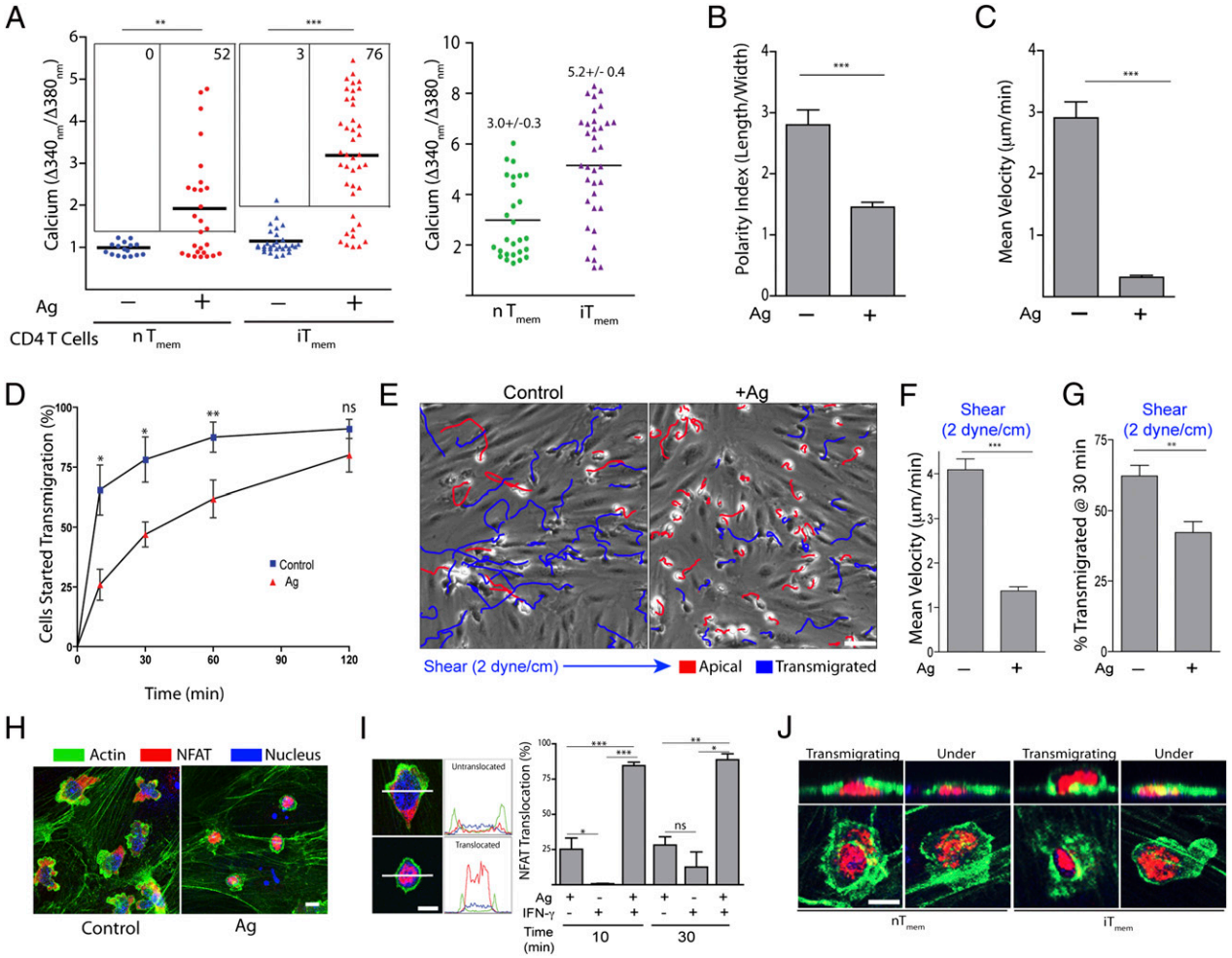

FIGURE 1. Human microvascular ECs are capable of Ag-specific stimulation of CD4 memory-like T cells. (**A**) Human CD4 nT_{mem} (circles) or iT_{mem} (triangles) were loaded with Fura-2 and incubated on Ag-pulsed HLMVECs. Calcium flux at 5 min (*left*) or at maximal value over a 30-min duration (*right*) were plotted. (**B** and **C**) iT_{mem} were incubated on HLMVEC pulsed with Ag and T cell polarity (length/width ratio) at 5 min, and velocity was calculated over a 30-min duration. (**D**) iT_{mem} transendothelial migration was scored on Ag pulsed ECs as described in *Materials and Methods*. (**E**) iT_{mem} were infused over Ag-pulsed HLMVEC at 2 dyne/cm^2 and imaged. Depicted is an end-point image with migration tracks of apical (blue) and transmigrated (red) lymphocytes. See also Supplemental Video 1. (**F** and **G**) Lateral migration velocities for T cells from (E) during both prediapedesis and postdiapedesis phases of migration over 30 min (F) and percentage of iTmem transmigrated were measured (G). (**H**) Representative images of nT_{mem} incubated on Ag-pulsed HLMVEC and staining for actin (green), NFAT (red), and nucleus (blue). (**I**) nT_{mem} were incubated on activated HLMVEC. Nuclear NFAT translocation was scored according to line scan profiles (*left*). (**J**) Samples were acquired as in (H), and representative transmigrating or transmigrated ('Under') lymphocytes are shown. Data represent mean ± SD (B, C) or SEM (D, F, G, I). Scale bars, 5 μm. $*p < 0.05$, $**p < 0.005$, $***p < 0.0005$.

Next, we set up live-cell analysis to concomitantly monitor T cell activation (i.e., calcium flux) and migration on endothelium pulsed with Ag (i.e., bacterial superantigen, a widely used model Ag) (38, 40, 41). In the absence of Ag, nT_{mem} and iT_{mem} fluxed little calcium (Fig. 1A), remained polarized (Fig. 1B), and underwent continuous lateral (Fig. 1C) and transendothelial migration (i.e., "diapedesis"; Fig. 1D). On HLMVECs pulsed with Ag (1 μg/ml SEB and TSST), T cells rapidly fluxed calcium, lost polarity, and arrested migration (Fig. 1A–C). Similar results were found with alternate Ag (e.g., SEE and MAM) presented by HDMVECs or HUVECs (Supplemental Fig. 1D and data not shown). In addition, in the absence of Ag, the majority of iT_{mem} transmigrated within 30 min, whereas in the presence of Ag, diapedesis was delayed by ~30–60 min (Fig. 1D). Thus, the migratory stop signal was transient. IT_{mem} also exhibited Ag-dependent transient migration arrest under conditions of laminar fluid shear flow conditions similar to those found in microvasculature in vivo (2 dyne/cm^2; Fig. 1E–G, Supplemental Video 1).

During T cell activation, the transcription factor NFAT translocates from the cytoplasm to the nucleus. Incubation of nT_{mem} on

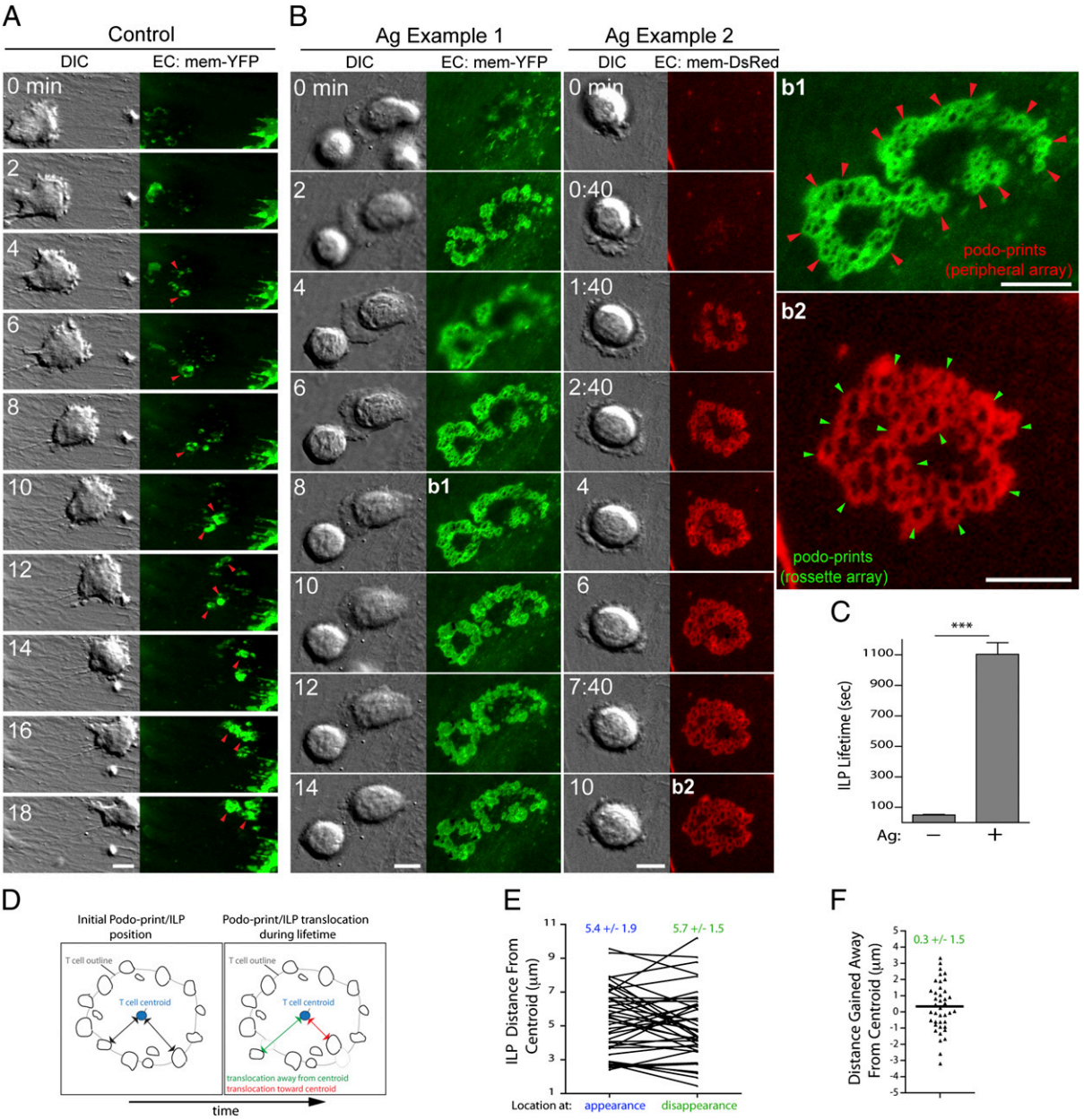

FIGURE 2. CD4 memory-like T cells form stabilized arrays of ILPs on Ag-presenting endothelium. (**A** and **B**) HLMVECs were transfected with mem-YFP or mem-DsRed, activated, and pulsed without (A) or with (B) Ag (TSST/SEB). iT_{mem} were imaged live on addition to ECs. Individual frames at selected time intervals are shown. Arrows indicate fluorescent rings formed on endothelium under adherent lymphocytes. The corresponding control (A) and Ag (**b1** and **b2**) videos are provided as Supplemental Videos 2–4, respectively. (**C**) Podo-print/ILP lifetimes from imaging studies as in (A) and (B). Data represent mean ± SEM of at least 80 ILPs formed by at least 25 cells from ≥3 separate experiments. (**D**) Schematic representation of podo-print/ILP lateral translocation analysis. Gray "T cell outline" represents a T cell–EC contact area with the "T cell centroid" indicated as a blue circle and individual podo-prints indicated as black rings. The linear distance between the centroid and podo-print was measured at both the first and last appearance of an individual podo-print/ILP during its lifetime. (**E** and **F**) Podo-print/ILP distances were measured as in (D). Distances from the cell centroid at time of formation and disappearance were plotted for individual podo-prints (E). Data from (E) was further processed to report change in distance (F). Scale bars, 5 μm. ***$p <$ 0.0005.

Ag-pulsed ECs promoted robust nuclear translocation of NFAT (Fig. 1H, 1I). Significantly, transmigrating nT_{mem} and iT_{mem} retained nuclear NFAT, demonstrating that these cells remained activated (Fig. 1J). NT_{mem} on endothelium that was pulsed with Ag but not pretreated with IFN-γ (and therefore lacked strong MHC-II expression) exhibited little NFAT translocation (Fig. 1I), confirming that the responses to Ag-pulsed endothelium were MHC-II dependent.

To show that T cells achieved complete activation, we conducted studies using a transwell system, in which T cells loaded into an upper chamber migrated across an EC monolayer to reach the lower chamber. Flow cytometry revealed that after migrating across Ag-pulsed ECs, iT_{mem} showed increased surface expression of CD69 and a reduction in CD62L (Supplemental Fig. 1E). In addition, in these nonpolarizing conditions, a subset of the iT_{mem} upregulated IFN-γ expression (Supplemental Fig. 1F, 1G) and increased proliferation (Supplemental Fig. 1H). Collectively, these results demonstrate that endothelium is able to present model Ag in an MHC-II–dependent manner to CD4 memory/effector lymphocytes, which induces a transient delay in diapedesis and T cell activation.

ILP arrays dominate the T cell–EC interface during activation

Next, we investigated the cellular and molecular basis for T cell activation in our endothelial APC model. Previously, we used fluorescent membrane markers (mem-YFP or mem-DsRed) expressed in the ECs to detect topological changes in the plasma membrane (34). In this way, we demonstrated that ~0.5-μm fluorescent rings that formed dynamically on the endothelium under migrating T cells corresponded to cylinder-shaped cell surface invaginations (i.e., "podo-prints") induced by lymphocyte ILPs. Thus, podo-prints formed on the EC surface served as an indirect but sensitive readout for T cell ILPs (34). In this study, we similarly observed in control settings that podo-prints formed and disappeared

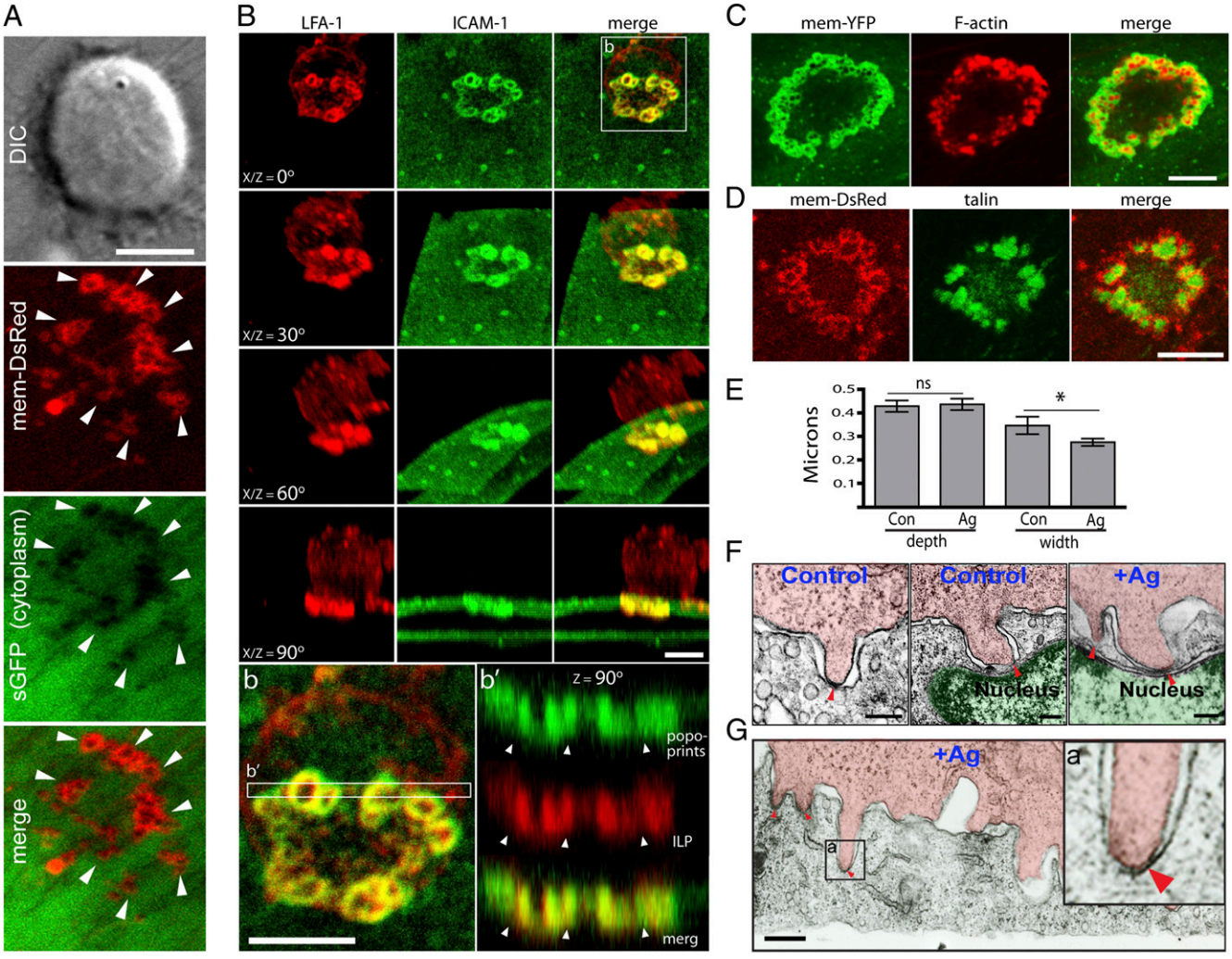

FIGURE 3. Ag-stabilized ILPs exhibit a discrete three-dimensional architecture. (**A**) Ag-stabilized T cell ILPs protrude into the EC surface. Imaging was conducted as in Fig. 2B on HLMVECs coexpressing soluble, cytoplasmic GFP (green) and mem-DsRed (red). (**B**) Three-dimensional reconstruction from confocal imaging of podo-prints and ILPs. iT_{mem} were incubated for 20 min on activated Ag-pulsed (SEE) HUVECs and then fixed, stained for ICAM-1 (green) and LFA-1(red), and imaged by confocal microscopy. Sections were digitally reconstructed and projected as three-dimensional renderings. (**b**) Magnified view of the ILP arrays. (**b′**) Orthogonal cross section. See also Supplemental Video 5. (**C** and **D**) Ag-stabilized ILPs are enriched in actin and talin. Mem-YFP–transfected (C; green) or mem-DsRed–transfected (D; red) HLMVECs were pulsed with Ag (TSST/SEB) and incubated with iT_{mem} for 5 min and stained for F-actin (C; red) or talin (D; green). (**E**) Quantitation of ultrastructural depth and width of T cell ILPs. Samples as in (C) were imaged by electron microscopy and ILPs were measured. Data represent mean ± SEM from at least 100 ILPs from at least 20 representative micrographs per condition. (**F** and **G**) ILPs enforce close T cell–EC membrane apposition in the absence and presence of Ag. T cell and endothelial nuclei are indicated with red and green overlays, respectively. Arrows and (**a**) highlight regions of extremely close lymphocyte–EC membrane apposition enforced at the ILP tips. Scale bars, 5 μm (A–D); 500 nm (F, G). *$p < 0.05$. ns, Not significant.

continuously (with lifetimes of tens of seconds) under the leading edge lamellipodia of migrating iT_{mem} (Fig. 2A, 2C, Supplemental Video 2). Strikingly, when ECs were pulsed with Ag, iT_{mem} rapidly formed dense arrays of podo-prints largely localized at the periphery of the T cell–EC interface under symmetrical lamellipodia (Fig. 2B, example 1, and Supplemental Video 3). A minority (~20–30%) of the iT_{mem} cells formed rosette-type podo-print arrays that lacked bias for the cell periphery (Fig. 2B, example 2, and Supplemental Video 4). In both cases, podo-prints/ILPs were significantly stabilized (lifetimes of ~18 min; Fig. 2C) and exhibited limited lateral translocation (0.31 ± 1.5 μm; Fig. 2D–F). After ~30 min of contact, ILPs began to disappear and T cells initiated transmigration (Supplemental Video 4 and data not shown).

As confirmation that the earlier observations reflected three-dimensional podo-prints in response to T cell ILPs, we cotransfected endothelium with mem-DsRed together with soluble GFP as a marker for cytoplasmic volume (34). This showed individual fluorescent membrane rings of each podo-print, in fact, represented cytosol-displacing invaginations into the EC surface (Fig. 3A). Furthermore, confocal imaging showed that podo-prints were ICAM-1–enriched cylindrical EC invaginations into which T cell ILPs extended (Fig. 3B, Supplemental Video 5). ILPs were enriched in LFA-1 (Fig. 3B), F-actin (Fig. 3C), and talin (Fig. 3D), similarly to invadosomes (35, 36). Analogous structures formed under physiologic shear flow (Supplemental Fig. 2A), with diverse ECs (including HLMVECs [Fig. 3A, 3C, 3D], HUVECs [Fig. 3B], HDMVECs [data not shown]), with nT_{mem} (Supplemental Fig. 2B), and with alternate Ag (Fig. 3B, Supplemental Fig. 2D). Similar structures also formed when previously activated murine OT-II $CD4^+$ T cells were incubated on heart microvascular ECs pulsed with OVA 323–339 peptide Ag (Supplemental Fig. 2E).

To assess the T cell–EC interaction in greater detail, we used transmission electron microscopy. In the absence of Ag, ILPs averaged 430 ± 34 nm in depth and 348 ± 33 nm in width (Fig. 3E, 3F). In the presence of Ag, ILPs were similar in morphology and size (depth = 437 nm, width = 277 nm), but tended to form in denser clusters (Fig. 3E–G). An important feature of the ILPs, whether in the absence or presence of Ag, was the existence of zones of extremely close T cell–EC apposition, typically at the tips of the ILPs as if driven by ILP extension (Fig. 3F, 3G, arrows). Although not exclusive to these locations, quantitative analysis revealed that intercellular contacts of <20 nm were 9-fold greater at ILP tips compared with other regions. The idea that ILPs can exert significant force is supported by their ability to both drive

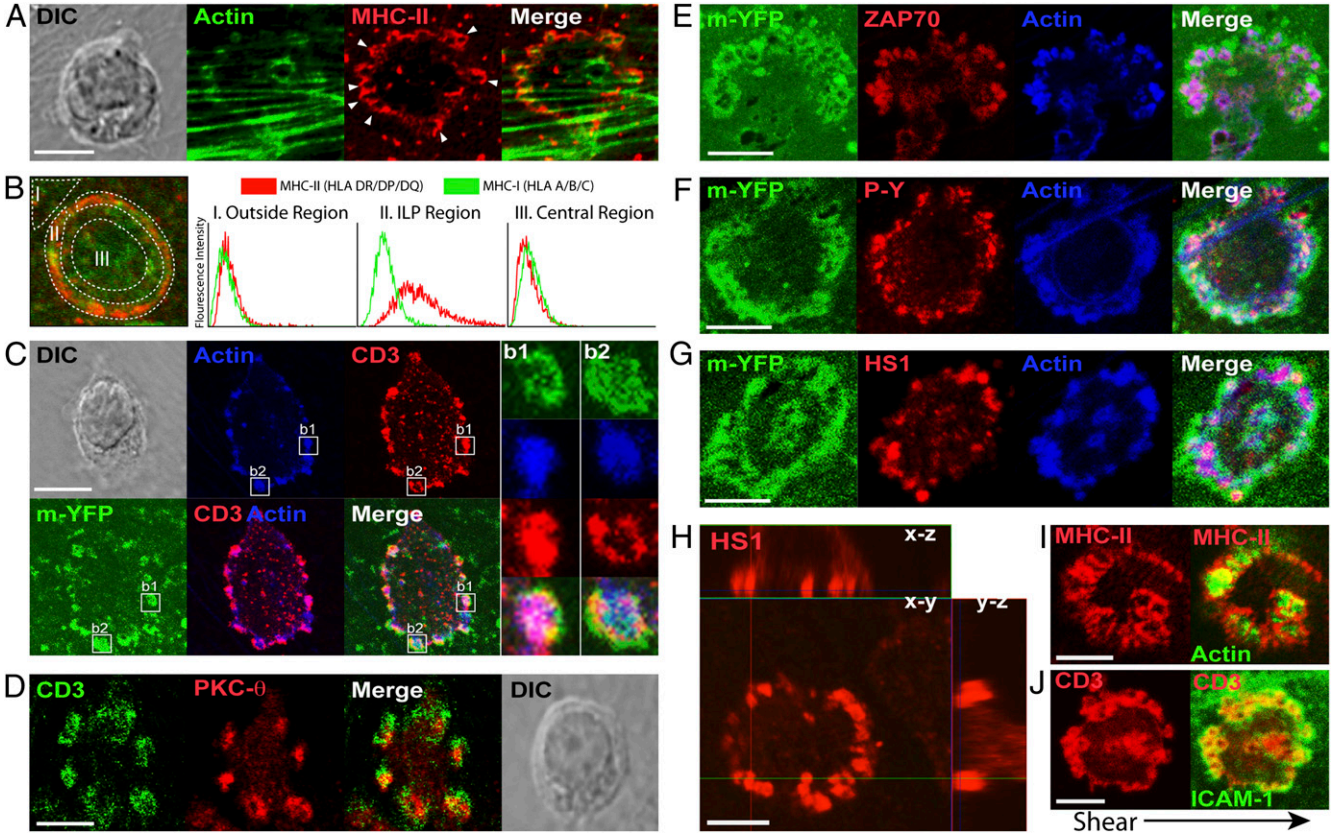

FIGURE 4. Ag-stabilized ILPs are foci for immune signaling. IT_{mem} cells were incubated with activated, Ag-pulsed (TSST/SEB) HLMVEC for 5 min, fixed, and stained as indicated and imaged by confocal microscopy. (**A**) Ag-stabilized ILPs (F-actin, green) protrude into MHC-II (red)–enriched podo-prints. Arrows indicate MHC-II–enriched podo-prints. (**B**) Samples as in (A) were stained for MHC-II (HLA-DR/DP/DQ; red) and MHC-I (HLA A/B/C; green). Schematic of gated regions of interest is shown on the *left* and included a region outside of the IS (I), the ILP-rich region of the IS (II), and the central region of the IS (III). *Right panels* show pixel fluorescence intensity histograms for regions I–III. (**C**) ILPs (F-actin, blue) protruding into podo-prints (mem-YFP, green) are enriched in CD3 (red). Within individual ILPs, CD3 is predominantly focused at the tip (**b1**) and, to a lesser extent, the edge (**b2**). (**D**) PKC-θ (red) is enriched with CD3 (green) in ILPs. (**E**–**G**) ILPs (F-actin, blue) colocalize with ZAP70 (E; red), phosphotyrosine (F; red), and HS1 (G; red). (**H**) HS1 (red) is highly enriched in ILPs. Cross-sectional views from serial-section confocal microscopy are shown of a lymphocyte adherent to the endothelium-presenting Ag. See three-dimensional rotation in Supplemental Video 6. (**I** and **J**) ILP arrays were allowed to form as above with the additional presence of physiologic laminar fluid shear flow (2.0 dyne/cm^2; arrow indicates direction). (I) MHC-II (red) and F-actin (green) are shown. (J) CD3 (red) and ICAM-1 (green) are shown. Scale bars, 5 μm.

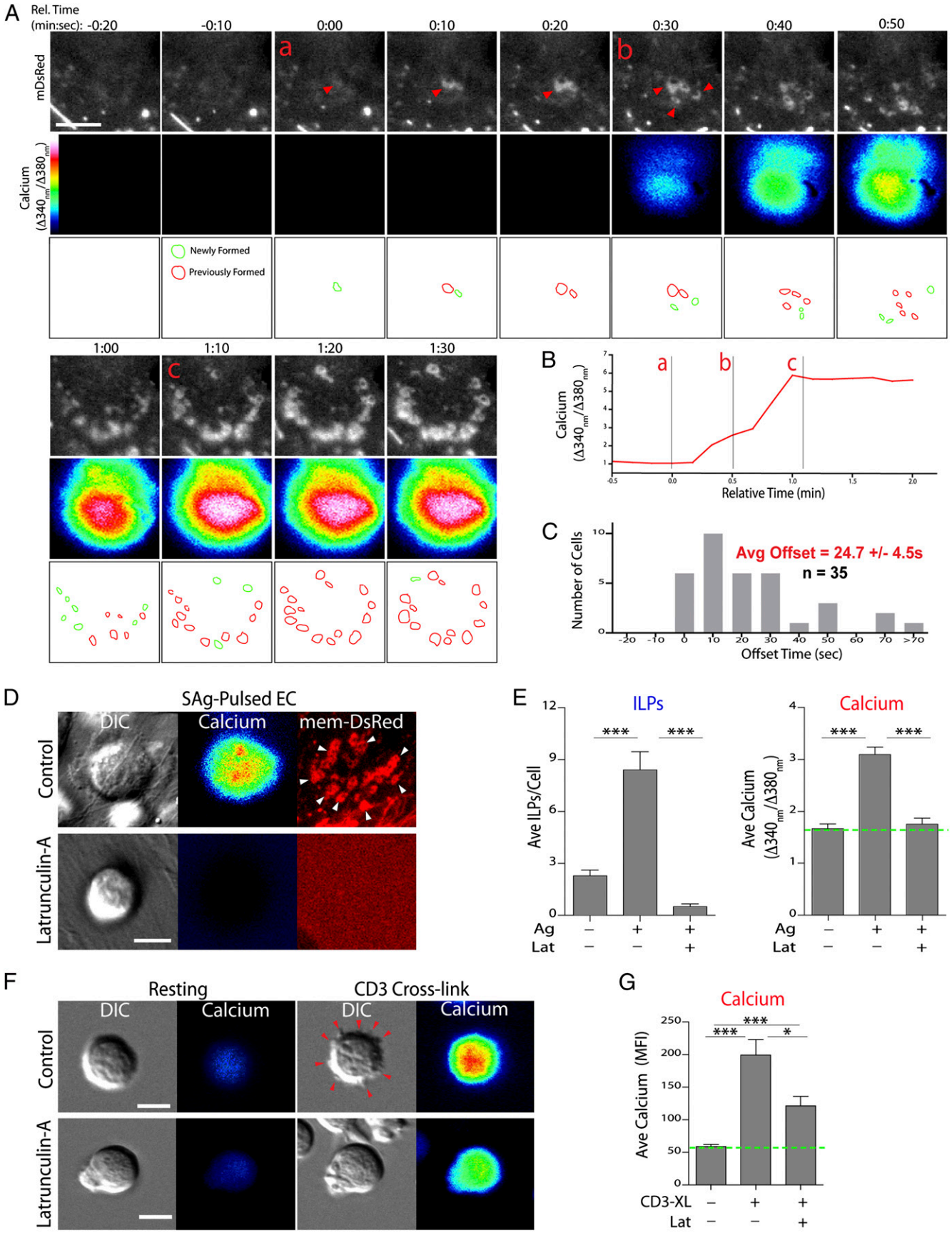

FIGURE 5. T cell ILP formation precedes and supports efficient Ag recognition. (**A**) IT_{mem} were labeled with Fura-2 and imaged live (at a maximal temporal resolution of 10 s) during migration on mem-DsRed–transfected, Ag-pulsed HLMVECs. *Upper panels* show mem-DsRed. Arrows indicate initial ILP formation. *Middle panels* indicate calcium flux values on a rainbow scale. *Lower panels* provide a schematic representation of newly formed (green) and previously formed (in relation to previous field; red) podo-prints. (**a**) Frame of initial ILP/podo-print. (**b**) Frame when calcium flux rises above background. (**c**) Frame when the peripheral ILP array is stabilized. Note this correlates with peak calcium flux. See also (*Figure legend continues*)

transcellular diapedesis (34) and to displace/deform organelles such as the nucleus (Fig. 3F).

Ag-stabilized ILPs share features of traditional TCR signaling microclusters

To address how these ILP-dominated cell–cell interfaces relate to TCR signaling, we stained for traditional IS markers (15, 20, 21). Confocal microscopy revealed that podo-prints on endothelium were modestly, but consistently, enriched in MHC-II compared with MHC-I or mem-YFP (Fig. 4A, 4B, Supplemental Fig. 3A), whereas T cell ILPs were enriched in CD3 (Fig. 4C, Supplemental Fig. 3B). Comparable enrichment formed under physiologic shear flow (Fig. 4I, 4J). In <5% of T cells, CD3 was distributed into a central supramolecular activation cluster-like cluster rather than in peripheral ILPs (Supplemental Fig. 3C).

Molecules implicated in TCR signaling, including PKC-θ (Fig. 4D, Supplemental Fig. 3D), ZAP70 (Fig. 4E), and phosphotyrosine (Fig. 4F) were also enriched in ILP cores, suggesting active signaling at these sites. The cortactin homolog HS1, a known regulator of both podosomes and ISs (38, 42–44), showed particularly strong enrichment (Fig. 4G, 4H, Supplemental Video 6). Alternatively, the inhibitory molecules CD43 and CD45 localized primarily to the region outside of the T cell–EC interface (Supplemental Fig. 3B). These observations suggest that ILPs may serve as discrete loci for TCR signaling with general features similar to TCR signaling microclusters and "multifocal" synapses (15, 21, 22, 45–47).

Collectively, these experiments show that CD4 iT_{mem} activation caused by EC MHC-II/Ag is coupled to cell–cell interfaces dominated by arrays of ILPs that are enriched in TCR signaling molecules. We term this previously undescribed architecture, which shares features of both podosome belts/rosettes and multifocal ISs, a "podo-synapse."

ILPs support efficient Ag recognition and sustained signaling

To determine the functional relationship between ILP formation and T cell activation, we concomitantly monitored calcium flux and ILP dynamics. In the presence of Ag, calcium flux was evident shortly after the first appearance of ILPs. It then peaked several minutes later and gradually decayed over the following 5–60 min (Fig. 5A, 5B, Supplemental Video 7). Calcium flux always occurred subsequent to (or in the same 10-s interval as) the appearance of at least one ILP, with an average offset time of ~25 s (Fig. 5C). In turn, stabilized ILP arrays and symmetric lamellipodia became evident in the ~30–60 s following the increase in calcium (Fig. 5A, 5B, Supplemental Video 7).

These observations suggested that the close intercellular contacts driven by ILPs may promote initial Ag recognition and TCR triggering. Testing this hypothesis is challenging because both ILPs and TCR signaling are fundamentally dependent on F-actin assembly and many of the same actin regulatory pathways (34, 35, 38, 42–44, 48). Thus, we simply compared effects of F-actin inhibition (via latrunculin A) on T cell activation through an Ag-pulsed APC versus direct TCR cross-linking. When stimulated by Ag-pulsed ECs, iT_{mem} pretreatment with latrunculin A caused 100% blockade of both ILP formation and calcium flux during the first 5 min of coincubation (Fig. 5D, 5E). By contrast, when TCRs were stimulated directly by anti-CD3/CD28 cross-linking, significant (although attenuated by ~60%), immediate calcium flux was elicited in the presence of latrunculin A (Fig. 5F, 5G), as shown previously (49). From this we conclude that the total latrunculin A-induced blockade of early response to Ag-pulsed ECs reflects a defect in initial Ag recognition/TCR triggering (Fig. 5F, 5G). We speculate that ILP formation may represent the latrunculin A-sensitive process behind this defect.

Calcium flux is necessary and sufficient for Ag-mediated ILP stabilization

Next, we investigated the transition from dynamic ILP probing to formation of stable ILP arrays. Given the correlation between increase in calcium and appearance of ILP arrays, we hypothesized that calcium may be key for stabilizing ILPs. To test this, we pretreated T cells with the calcium chelator BAPTA and the CRAC channel inhibitor BTP2. On Ag-pulsed ECs, this greatly inhibited calcium flux in iT_{mem}, which correlated with strong reduction in the number of stabilized ILPs (Fig. 6A–C). To determine whether calcium flux was sufficient to stabilize ILPs, iT_{mem} were incubated on ECs in the absence of Ag, followed by application of thapsigargin to directly increase intracellular calcium. This caused iT_{mem} already engaged in dynamic ILP probing to arrest migration and stabilize ILP clusters (Fig. 6D–G). Thus, whereas dynamic ILP probing of ECs by iT_{mem} seems to facilitate initial Ag recognition, the resulting increase in calcium is both necessary and sufficient to drive accumulation/stabilization of ILPs into podo-synapses.

The earlier findings point to a positive feedback loop for sustaining TCR signaling. To break this loop, we sought to block proximal signaling downstream of calcium flux, specifically targeting CAMKII via the inhibitor CK59 (50). Treatment with CK59 attenuated Ag-mediated ILP stabilization by ~50% (Fig. 6H), which was coupled to a proportional decrease in calcium flux (Fig. 6I). This result supports the interdependence between ILPs and calcium flux.

CD8 CTLs use ILPs to probe for Ag

The endothelium has been shown to initiate MHC-I/Ag-dependent activation of CD8 CTLs leading to direct killing of ECs (31, 32). To investigate these responses, we incubated previously activated murine OT-I CD8 T cells on murine heart microvascular ECs pulsed with SIINFEKL peptide Ag. Ag-pulsed ECs initiated a rapid calcium flux (Fig. 7A) that was coupled to progressive specific lysis of ECs over a 4-h duration (~50% lysis ~2 h; Fig. 7B). Live-cell imaging showed that in the absence of Ag, CTLs avidly probed the endothelium with dynamic ILPs while migrating without fluxing calcium (Fig. 7C, Supplemental Video 8). In the presence of Ag, initial ILPs were rapidly followed by calcium flux (offset time = 32.8 ± 6.6 s), which then led to migrational arrest and formation of peripheral ILP arrays similar to those formed by CD4 effector T cells (Fig. 7D, 7E). Thus, T cell ILPs seem to be a general feature of Ag sensing on ECs.

Supplemental Video 7. (**B**) Graphical representation of calcium flux with *frames a–c* noted. (**C**) Quantitation of ILP-calcium flux offset time. Live-cell imaging was as in (A) and offset time (time from when first ILP forms until calcium flux rises above background) was calculated. Data were binned into 10-s intervals, and average ± SEM is shown for 35 individual T cells from 3 separate experiments. (**D**) Imaging was performed as in (A) with additional pretreatment of T cells with latrunculin A before addition to Ag-pulsed EC monolayers. (**E**) Podo-print/ILP index (average number of podo-prints/ILPs per cell) and average calcium flux at 5 min was calculated. Both analyses are pooled mean ± SEM from three separate experiments. (**F**) IT_{mem} were labeled with Fluo-4 and imaged live with anti-CD3/CD28 cross-linking with or without latrunculin A pretreatment. *Left panels* show resting T cells. *Right panels* show activated T cells imaged 60 s after addition of cross-linking Abs. Arrows indicate de novo formation of micron-scale T cell protrusions. (**G**) Average calcium flux was calculated from three separate experiments as in (F). Scale bars, 5 μm. Data represent mean ± SEM. $*p < 0.05$, $***p < 0.0005$.

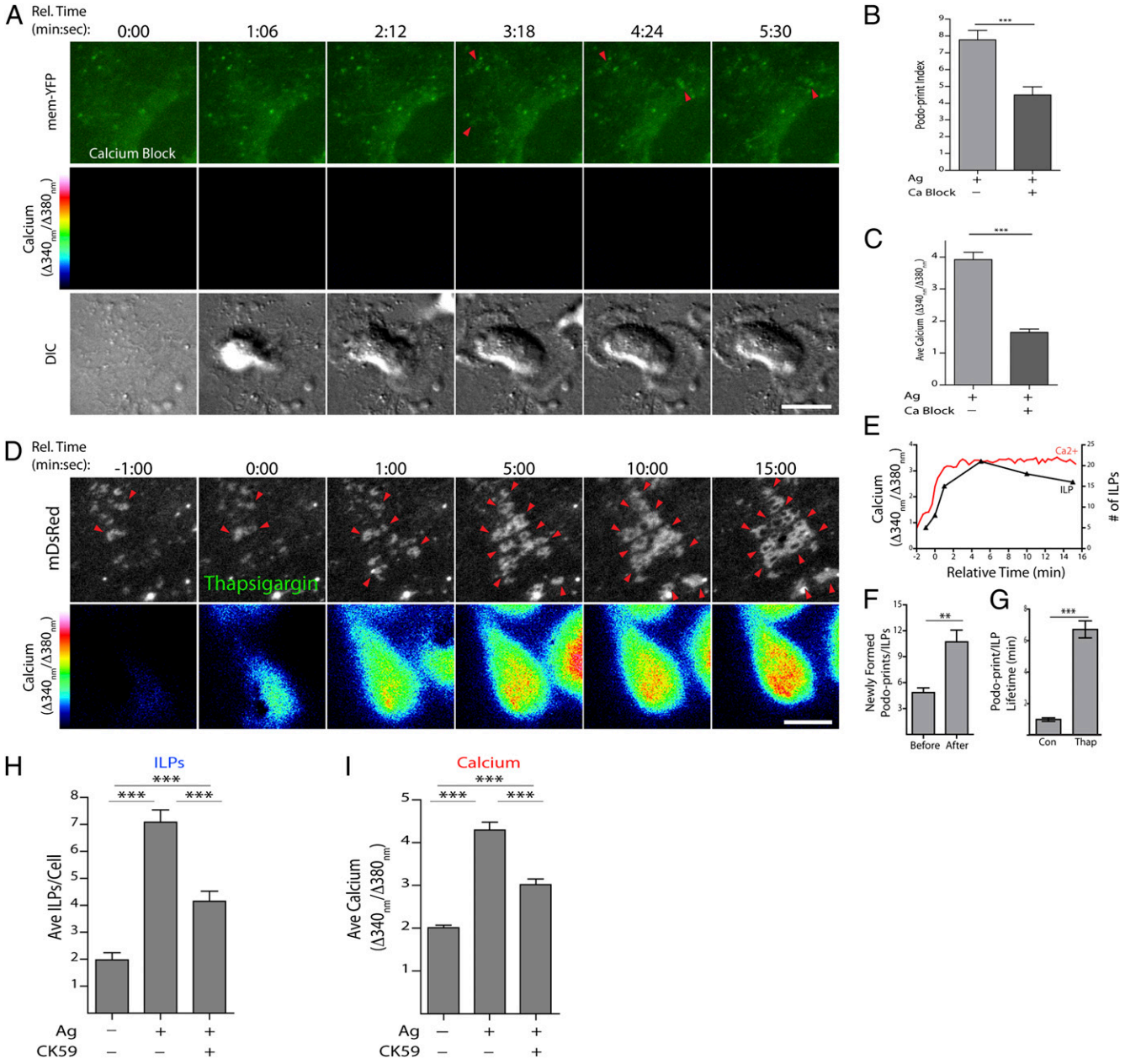

FIGURE 6. Calcium flux is necessary and sufficient for ILP stabilization. (**A**) IT_{mem} were Fura-2 labeled, pretreated with the calcium chelator BAPTA and the CRAC channel inhibitor BTP2, and imaged live on Ag-pulsed ECs. Arrows indicate a few sporadically formed podo-prints. (**B** and **C**) Podo-print/ILP index (B) and average calcium flux (C) were calculated at 5 min for experiments as in (A). (**D**) Live-cell imaging was conducted in the absence of Ag before and after addition of the calcium ionophore thapsigargin (at time = '0:00'). Arrows indicate ILPs/podo-prints. (**E**) Correlation of calcium flux with ILP number after addition of thapsigargin. (**F**) Quantitation of the number of newly formed ILPs in the 2 min before and after addition of thapsigargin. (**G**) Quantitation of the lifetime of ILPs with or without addition of thapsigargin. (**H** and **I**) Imaging and analysis was performed as in (A)–(C) except T cells were pretreated with the CAMKII inhibitor CK59. Data represent mean ± SEM. Scale bars, 5 μm. $^{**}p < 0.005$, $^{***}p < 0.0005$.

A planar-coated cell model for Ag recognition

We next considered whether ILPs either represent unique features of T cell-endothelial Ag recognition or may be more broadly relevant and uniquely revealed by endothelium. We speculated that the rigidity of coated substrate models may frustrate/mask ILP formation, whereas orientation/resolution issues might obscure detection of ILPs with traditional cellular APCs (16–18).

First, we simply asked whether evidence consistent with ILPs could be detected in a coated glass model (Fig. 8A). IT_{mem} plated on glass coated with ICAM-1 and anti-CD3 (but not anti-CD43/CD45) Ab rapidly fluxed calcium (Supplemental Fig. 4A–C). IRM revealed that initial "microcontacts" (~0.2- to 1-μm dots consistent with T cell ILPs and/or microvilli) always preceded calcium flux (Supplemental Fig. 4B, 4C; offset time = 21.4 s). New microcontacts also continued to form after T cell spreading (Fig. 8B, Supplemental Fig. 4D, 4E, Supplemental Video 9).

We hypothesized that these microcontacts at least partly reflected ILP activity that was mechanically frustrated by the rigid substrate. To test this, we designed a "coated-cell APC" model whereby the earlier Ab-coated glass substrate was recapitulated on the surface of a deformable CHO-K1 cell (Fig. 8C, Supplemental Fig. 4F). In this setting, clear three-dimensional ILP arrays were readily detected that were coupled to calcium flux (Fig. 8D, Supplemental Video 10). As with iT_{mem} on ECs, initial ILPs al-

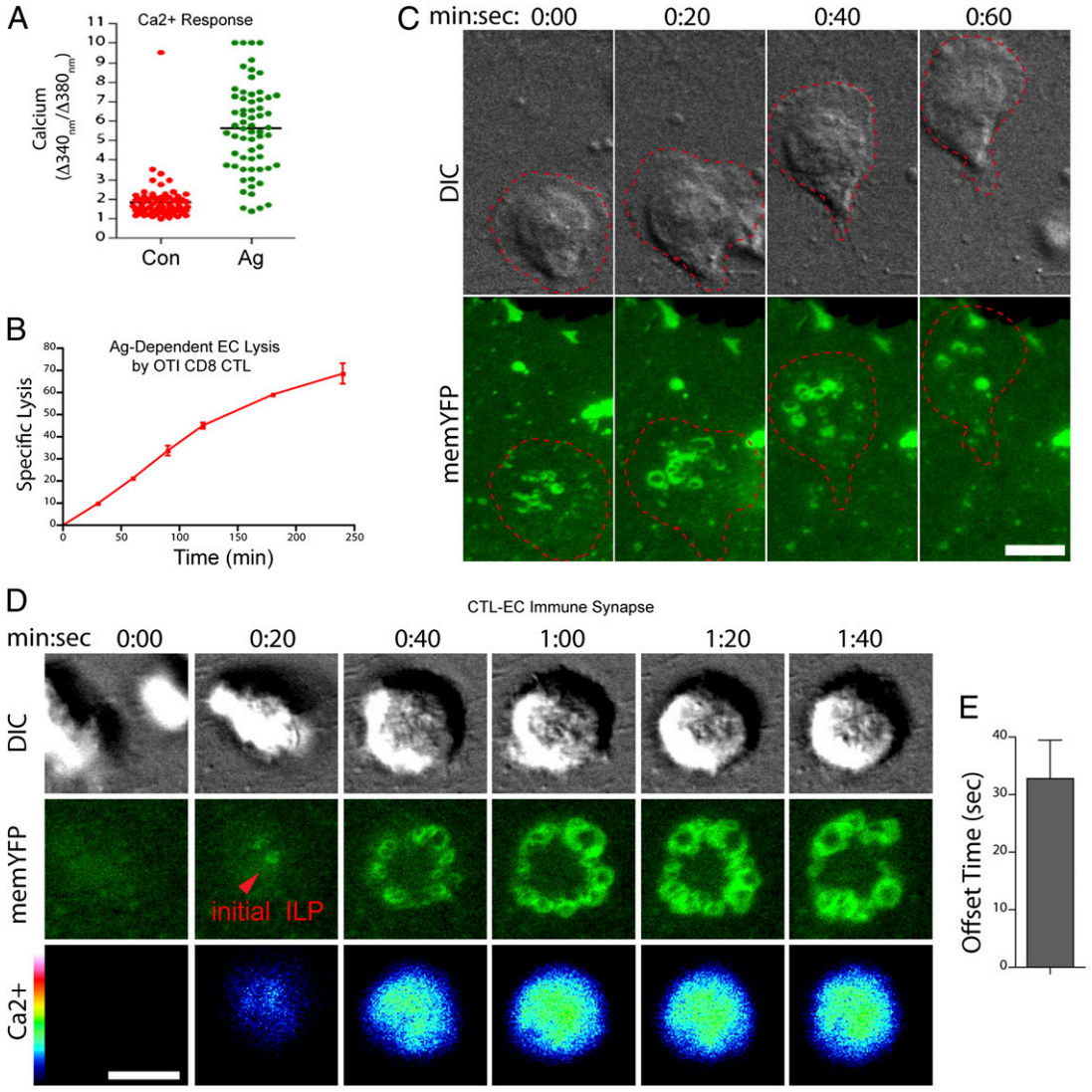

FIGURE 7. Murine CD8 CTLs use ILPs to sense Ag-bound MHC-I on endothelium. (**A**) Previously activated murine OTI CD8 T cells (CTLs) were imaged on mem-YFP–transfected, mouse heart microvascular ECs pulsed with SIINFEKL. Individual ratiometric calcium flux values at 5 min were plotted for ±Ag conditions. (**B**) CTLs were added to mixed cultures of Ag-pulsed/unpulsed ECs, and percentage of specific lysis is plotted at indicated time points. (**C**) CTLs were imaged during EC probing in the absence of Ag. Differential interference contrast and mem-YFP are shown in the *upper* and *lower panels*, respectively. Dashed line represents the outline of the migrating CTL under which transient ILPs are continuously formed. See also corresponding Supplemental Video 8. (**D**) Imaging was conducted as in (C) on ECs pulsed with SIINFEKL. Red arrow indicates initial ILP formation preceding calcium flux. (**E**) Average offset time for calcium flux relative to initial ILP formation. Data represent mean ± SEM. Scale bars, 5 μm.

ways preceded (Supplemental Fig. 4G; offset time ~56 s) and seemed to functionally support (Fig. 8E, 8F) initiation of calcium flux. These findings suggest a general tendency of memory/effector T cells to use ILPs to probe diverse substrates for recognition and response to Ag (as modeled in Fig. 9).

ILPs are involved in recognition of Ag presented by professional APCs

Next, we re-examined Ag recognition with professional APCs. Thus, iT_{mem} were incubated with Priess B cells pulsed with Ag and imaged by confocal microscopy. Equatorial cross sections recapitulate classic views (12) of the T cell–B cell IS whereby T cell LFA-1 shows enrichment in peripheral-supramolecular activation cluster–like peripheral membrane bulges (Supplemental Fig. 4H, *inset* 2, arrows). Cross sections taken at the edge of the IS additionally suggest presence of LFA-1–rich finger-like protrusions (Supplemental Fig. 4H, *insets* 1a–d) similar to ILPs formed on ECs (Fig. 3Bb). More compelling imaging of putative ILPs can be seen in occasional examples where the T cells settle on top of B cells such that the IS aligns with the optimal imaging plane (18) (Fig. 8G, Supplemental Video 11). Ultrastructural views, evident in a subset of micrographs, further support the presence of ILPs (Fig. 8H).

Finally, we investigated murine OTII CD4 T cells incubated with BMDCs coexpressing mem-YFP and soluble DsRed. T cells interacted with DCs both laterally (Fig. 8I, subset a) and to a lesser extent through en face contacts (Fig. 8I, subset b). In the former, side views of DC invaginations were readily evident that were similar to podo-prints/ILPs seen on endothelium (Fig. 8I, *panel* 3i). En face interactions also revealed discrete circular podo-prints/ILPs (Fig. 8I, *panels* 3ii, 3iii), although these were generally less obvious than those formed on endothelium because of the highly active and irregular surface topology of DCs. Dynamic imaging showed ILP probing preceded calcium flux, which, in turn, was coupled to peripheral ILP array formation (Fig. 8J). Ultrastructural confirmation of ILP formation could also be obtained

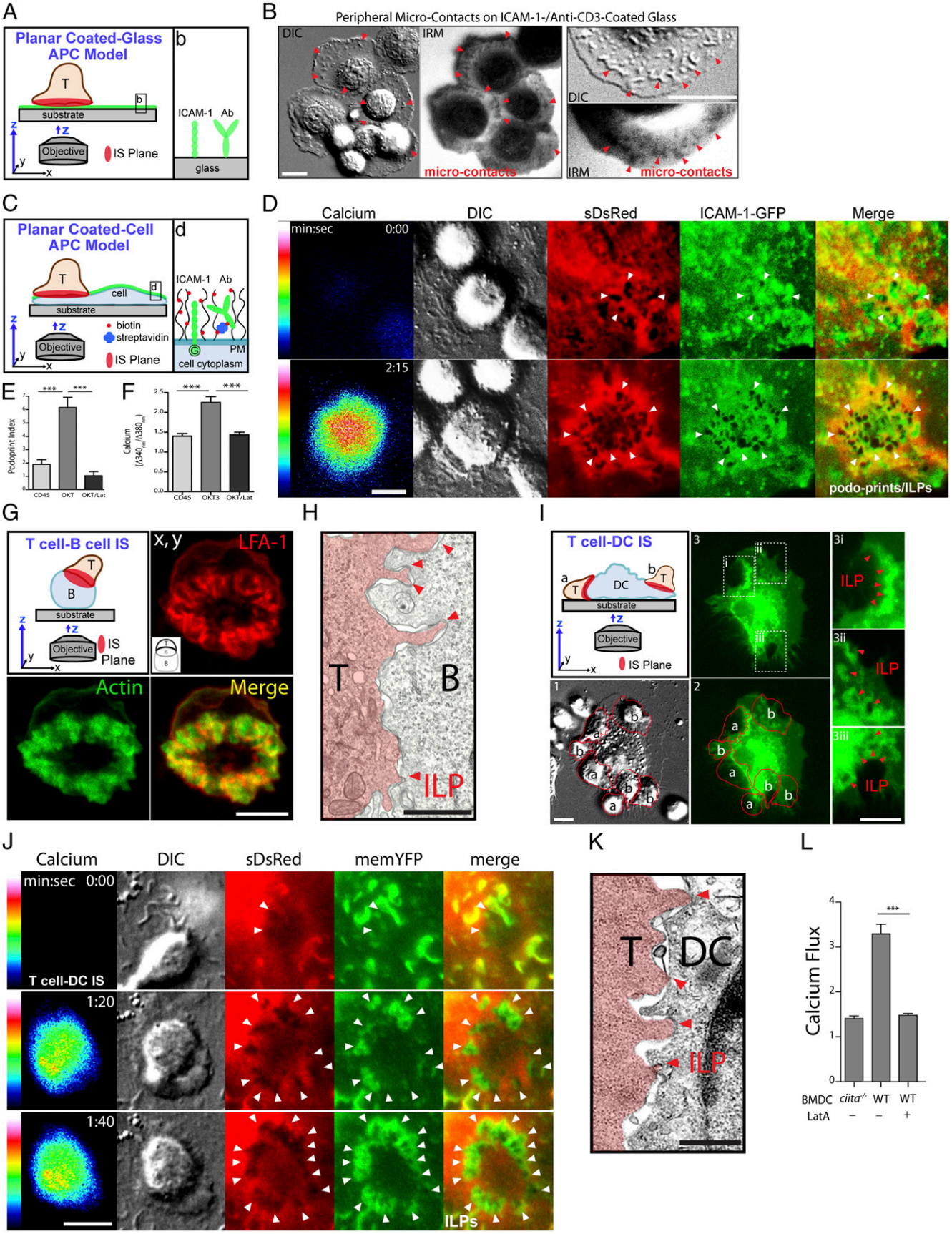

FIGURE 8. ILPs facilitate Ag recognition on professional APCs. (**A**) Schematic of the "coated-glass model" using ICAM-1– and Ab-coated glass. (**b**) Magnified view of the interaction surface. (**B**) iT_{mem} were added to an ICAM-1–Fc– and anti-CD3–coated glass chamber and imaged by differential interference contrast and IRM. Arrows indicate IRM-detected "microcontacts." (**C**) Schematic of the "planar coated-cell APC model." CHO-K1 cells expressing ICAM-1–GFP and soluble DsRed were surface "coated" with Abs against CD3, CD43, or CD45 using a biotin/SA capture approach (see also Supplemental Fig. 4F). (**d**) Magnified view of the interaction surface. (**D**) Cells prepared as in (C) coated with anti-CD3 Ab were (*Figure legend continues*)

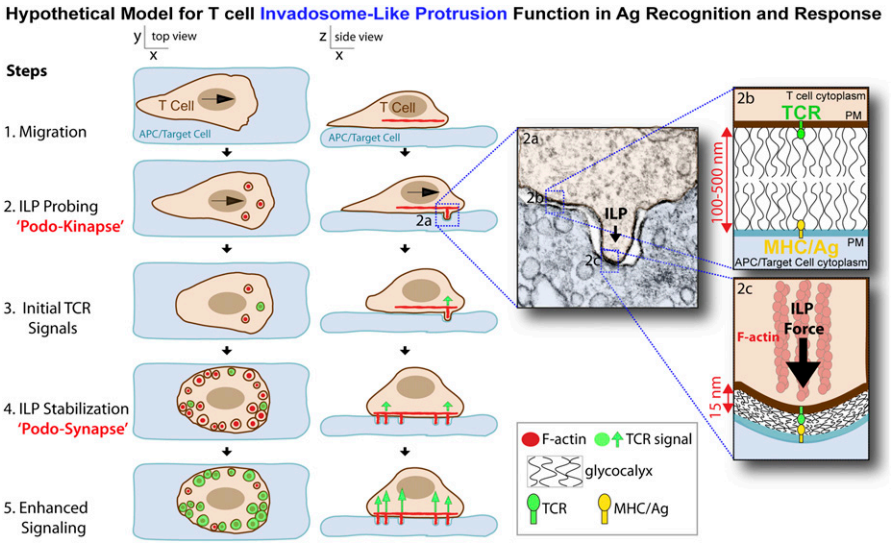

FIGURE 9. Hypothetical model for ILP function in Ag recognition and response. Schematic depicts top-down and side views of a memory/effector T cell interacting with an APC/target cell. Lymphocytes initiate lateral migration (Step 1) and begin to dynamically drive ILPs against the apposing cell (Step 2, **2a**). Close interactions between T and APC/target cells, which are partially opposed by the cell glycocalyces (**2b**), form preferentially (but not exclusively) at ILP tips (**2c**). We hypothesize that TCR/MHC interactions may be facilitated in these zones. Initial calcium released on Ag recognition (green overlay/arrows; Step 3) seems to be coupled to stabilization/accumulation of ILP arrays ("podo-synapses"; Step 4), which we hypothesize could, in turn, help sustain/enhance signaling (Step 5).

in a subset of electron micrographs (Fig. 8K). Finally, treatment of T cells with latrunculin A strongly inhibited both ILPs and initial calcium responses to Ag presented by DCs (Fig. 8L).

Discussion

Basic cellular mechanisms by which lymphocytes effectively scan for peptide Ag on apposing cells and how this leads to IS formation have remained mysterious. Our results investigating endothelium as a model APC indicate potential roles for ILPs in these processes. Our further studies with diverse Ag recognition settings suggest broad, previously unappreciated functions for ILPs as actuators of immune surveillance.

Vascular ECs represent intriguing and understudied APCs/target cells for adaptive immune responses. These MHC-I–, MHC-II–, and costimulator-expressing cells are strategically positioned at the blood–tissue interface to serve as unique sentinels for the immune system (26). Previous studies demonstrated that ECs can effectively restimulate memory/effector, but not naive, T cells (26–33). Thus, ECs have been hypothesized to serve as peripheral ancillary or "semiprofessional" APCs that contribute to the effector phase of adaptive immune responses. Although overall roles remain controversial, studies suggest that Ag presentation by ECs can influence T cell activation, differentiation, trafficking, and memory (26–28, 51). In this study, we demonstrate that CD4 and CD8 memory/effector T cells exhibited a transient arrest in migration coupled, respectively, to Th1 and cytotoxic responses on ECs presenting MHC/Ag, consistent with previous findings (31, 52, 53).

Importantly, ECs exhibit a virtually planar cell surface in vitro, which we previously established to be ideal for high spatiotemporal resolution imaging of topological dynamics (34). We reasoned that ECs might, therefore, serve as physiologic "planar APC/target cell" models uniquely suited to fill two key gaps in our understanding of immune surveillance mechanisms: 1) how initial MHC/Ag-sampling contacts form between T cells and APCs, and 2) how these lead to formation of productive ISs. Although planar APC substrates (i.e., lipid bilayers, Ab-coated glass) provide excellent imaging, which has led to critical insights to these dynamics (15, 19–22), such models are inherently limiting. Alternatively, details of physiologic cell–cell scanning dynamics are profoundly obscured by orientation-related imaging issues (16–18). The imaging afforded with our planar endothelial APC model in this study revealed unexpected involvement of ILPs in Ag recognition and response activities.

ILPs ("invadosome-like protrusions") are lymphocyte equivalents (36) to podosomes (formed largely by myeloid lineage cells) and invadopodia (formed by transformed cells), collectively termed "invadosomes" (35). Invadosomes and ILPs are actin-dependent cylindrical, protrusive organelles (~200–1000 nm in diameter and depth) that form on the ventral surface of migratory cells (35). Distinct from invadosomes, characterized to form on matrix, bone, glass/plastic substrates, T cell ILPs have only been seen on cellular substrates, as shown in a range of in vitro (34, 54, 55) and in vivo studies (reviewed in Ref. 56). In such settings, dynamic ILP probing seems to function in migratory pathfinding,

imaged live on addition of Fura-2–labeled iT_{mem}. *Panels* demonstrate relatively early and later phases of interaction as indicated. Arrows indicate podoprints/ILPs. See also Supplemental Video 10. (**E** and **F**) Imaging experiments were conducted as in (D), but T cells were pretreated with latrunculin A. Podoprint/ILP index (E) and calcium flux (F) were calculated. (**G**) IT_{mem} were incubated with Ag-pulsed Priess B cells for 5 min and stained for LFA-1 and actin. Image represents a three-dimensional projection of T cell settled on top of the B cells with the IS forming more nearly parallel to the *x*–*y* imaging plane. See also Supplemental Video 11. (**H**) Transmission electron micrograph of T cell–B cell IS as in (G). The T cell is identified by a red overlay. Arrows indicate close intercellular contacts formed by T cell ILPs. (**I**) Schematic (*upper left panel*) shows both lateral (a) and various en face (b) interfaces typically formed in vitro between T cells and the highly irregular surfaces of DCs. (**1**) and (**2**) show previously activated murine CD4 OT-II lymphocytes interacting with Ag-pulsed mem-YFP–transfected DCs (green, 2). Red outlines depict T cell perimeter based on DIC imaging (1). (**3**) is identical to (2) but shows three boxed regions (**i**–**iii**) expanded on the *left*. (3i) shows a lateral interaction in which the T cell has pushed small finger-like invagination into the side of the BMDC putatively formed by ILPs (arrows). (3ii) and (3iii) show en face interactions whereby ILPs seem to be extending normal to the imaging plane, giving rise to the typical ring-shaped podo-print appearance observed in endothelium (i.e., Fig. 2). (**J**) DCs were transfected with soluble monomeric DsRed and mem-YFP, pulsed with Ag, and CD4 OT-II T cells were added. *Panels* show cytoplasm displacing podo-prints/ILP (arrows), which precede calcium flux and are stabilized after calcium flux. (**K**) Transmission electron micrograph of T cell–DC IS as in (J) fixed after 5 min. The T cell is identified by a red overlay. Arrows indicate close intercellular contacts formed by T cell ILPs. (**L**) Calcium flux of previously activated CD4 OTII T cells 8 min after interaction with C57BL/6 (WT) or *Ciita*$^{-/-}$ Ag-pulsed DCs with or without latrunculin A pretreatment. Data represent mean ± SEM. Scale bars, 5 μm. ***$p < 0.0005$.

apparently serving as biomechanical sensors (34, 36, 54, 55, 57). These studies suggest that ILPs may also facilitate biochemical or "informational" scanning of diverse cell surfaces.

We speculated that the ILP scanning seen on ECs was uniquely revealed by this setting, rather than a unique feature of it. IRM imaging of a rudimentary APC model (anti-CD3–coated glass) showed that T cells form a series of microcontacts with the substrate that are consistent with either ILP or microvilli interactions. Similar microcontacts were previously shown to be enriched in F-actin, WASP, and TCR, and hypothesized to represent frustrated podosomes (20, 22). When we tested this hypothesis by recapitulating the same anti-CD3 activation stimuli on a pliable cell surface, we, indeed, found that the microcontacts transitioned into three-dimensional ILPs and podo-prints. Moreover, our studies using approaches optimized for imaging professional APCs (i.e., B cells and DCs) readily detected ILPs probing in these settings. Importantly, although dynamics, molecular composition, and three-dimensional architectures were not defined, extensive (largely EM-based) studies previously evidenced similar T cell protrusions extending against diverse APCs and target cell surfaces (21, 43, 58–63). Collectively, this suggests broad relevance for memory/effector T cells probing their cellular environment with ILPs. The important question of whether naive T cells similarly use ILPs remains to be addressed.

One possible role for ILP probing may be in enhancing the efficiency of Ag recognition. The act of Ag detection requires T cell and APC/target membranes to come within ~14 nm of each other (2, 64). Yet, all cell membranes are extensively shielded by ~50- to 500-nm-thick glycocalyces (3–5) that physically oppose close contact and negatively modulate immune recognition (5–10) (Fig. 9, *inset* 2b). In the periphery, patrolling effector/memory lymphocytes must effectively scan the surfaces of widely varying cell types (indeed, essentially any host cell could become a target), each with glycocalyces of different thicknesses and physicochemical properties. Forces provided by ILP (which form independently of Ag during lateral migration) (34) are sufficient to deform nuclear lamina, displace and distort cytoskeleton and intracellular organelles, and promote transcellular diapedesis (34). More than sufficient energy would, therefore, seem to be available at the tips of ILPs (Fig. 9, *inset* 2a) to overcome repulsion provided by the glycocalyx (Fig. 9, *inset* 2c).

Previous studies showed that lamellipodia of migrating lymphocytes are zones of heightened Ag recognition efficiency (65–67). In both our previous (34) and current work, we show that lamellipodia are also the predominant areas of ILP formation. Moreover, in our experimental system, ILPs, but not necessarily lamellipodia, consistently preceded calcium flux. Thus, although migration behaviors are necessary for immune surveillance, ILPs may function more directly in promoting intimate contacts, and thereby ensuring efficient Ag sampling. Our studies with latrunculin A are consistent with (although do not prove) such functional roles. It is also interesting to note that forces and membrane bending associated with ILPs are consistent with the hypothesized force-based mechanism for formal triggering of TCR signaling (22, 68–71). ILPs are probably not absolutely required for either TCR signaling or forming intimate T cell–APC/target contacts, but rather act to ensure efficiency and fidelity of immune surveillance.

Another possible function for ILPs may be to support signal amplification and sustenance. Our studies reveal dense arrays of calcium-stabilized ILPs that dominate the IS after Ag recognition. Individual ILPs showed enrichment in TCR and molecules suggestive of active signaling. This feature is generally not unlike TCR signaling microclusters defined using planar APC model substrates (14, 15, 20–22, 38, 72, 73), with the key distinction that ILPs have a discrete three-dimensional architecture. The well-developed concept that microclusters may function as "signalosomes" to amplify and sustain signaling by concentrating important molecules/activities might then be extended to include limited "reaction volumes" formed within ILPs (17, 74–78). In addition, the stable peripheral ILP arrays are strikingly similar to osteoclast "podosome-belts" (79, 80) that form sealing zones for directed secretion of bone-degrading enzymes (81). Thus, it may be hypothesized that peripheral podo-synapses may function analogously for directed secretion of cytokines or cytotoxic materials.

These studies collectively support the hypothesis that ILPs may serve as newly appreciated sensory organelles that facilitate Ag recognition and responses. By virtue of physical force exertion, ILPs literally allow T cells to get a deeper understanding of their local cellular environment. Such proactive "informational scanning" might ensure robust sampling of MHC/Ag on diverse cell types. It is tempting to speculate that stabilized TCR-enriched ILPs resulting from Ag recognition represent a clearer, more physiologic view of TCR microclusters and "multifocal" ISs characterized to date.

Disclosures

The authors have no financial conflicts of interest.

References

1. von Andrian, U. H., and C. R. Mackay. 2000. T-cell function and migration. Two sides of the same coin. *N. Engl. J. Med.* 343: 1020–1034.
2. Rudolph, M. G., R. L. Stanfield, and I. A. Wilson. 2006. How TCRs bind MHCs, peptides, and coreceptors. *Annu. Rev. Immunol.* 24: 419–466.
3. Weinbaum, S., J. M. Tarbell, and E. R. Damiano. 2007. The structure and function of the endothelial glycocalyx layer. *Annu. Rev. Biomed. Eng.* 9: 121–167.
4. Bell, G. I., M. Dembo, and P. Bongrand. 1984. Cell adhesion. Competition between nonspecific repulsion and specific bonding. *Biophys. J.* 45: 1051–1064.
5. Springer, T. A. 1990. Adhesion receptors of the immune system. *Nature* 346: 425–434.
6. Gubbels, J. A., M. Felder, S. Horibata, J. A. Belisle, A. Kapur, H. Holden, S. Petrie, M. Migneault, C. Rancourt, J. P. Connor, and M. S. Patankar. 2010. MUC16 provides immune protection by inhibiting synapse formation between NK and ovarian tumor cells. *Mol. Cancer* 9: 11.
7. Komatsu, M., L. Yee, and K. L. Carraway. 1999. Overexpression of sialomucin complex, a rat homologue of MUC4, inhibits tumor killing by lymphokine-activated killer cells. *Cancer Res.* 59: 2229–2236.
8. Tsuboi, S., and M. Fukuda. 2001. Roles of O-linked oligosaccharides in immune responses. *Bioessays* 23: 46–53.
9. van de Wiel-van Kemenade, E., M. J. Ligtenberg, A. J. de Boer, F. Buijs, H. L. Vos, C. J. Melief, J. Hilkens, and C. G. Figdor. 1993. Episialin (MUC1) inhibits cytotoxic lymphocyte-target cell interaction. *J. Immunol.* 151: 767–776.
10. Manjunath, N., M. Correa, M. Ardman, and B. Ardman. 1995. Negative regulation of T-cell adhesion and activation by CD43. *Nature* 377: 535–538.
11. Shaw, A. S., and M. L. Dustin. 1997. Making the T cell receptor go the distance: a topological view of T cell activation. *Immunity* 6: 361–369.
12. Monks, C. R., B. A. Freiberg, H. Kupfer, N. Sciaky, and A. Kupfer. 1998. Three-dimensional segregation of supramolecular activation clusters in T cells. *Nature* 395: 82–86.
13. Delon, J., S. Stoll, and R. N. Germain. 2002. Imaging of T-cell interactions with antigen presenting cells in culture and in intact lymphoid tissue. *Immunol. Rev.* 189: 51–63.
14. Brossard, C., V. Feuillet, A. Schmitt, C. Randriamampita, M. Romao, G. Raposo, and A. Trautmann. 2005. Multifocal structure of the T cell - dendritic cell synapse. *Eur. J. Immunol.* 35: 1741–1753.
15. Dustin, M. L. 2009. The cellular context of T cell signaling. *Immunity* 30: 482–492.
16. Balagopalan, L., E. Sherman, V. A. Barr, and L. E. Samelson. 2011. Imaging techniques for assaying lymphocyte activation in action. *Nat. Rev. Immunol.* 11: 21–33.
17. Cebecauer, M., M. Spitaler, A. Sergé, and A. I. Magee. 2010. Signalling complexes and clusters: functional advantages and methodological hurdles. *J. Cell Sci.* 123: 309–320.
18. Oddos, S., C. Dunsby, M. A. Purbhoo, A. Chauveau, D. M. Owen, M. A. Neil, D. M. Davis, and P. M. French. 2008. High-speed high-resolution imaging of intercellular immune synapses using optical tweezers. *Biophys. J.* 95: L66–L68.
19. Grakoui, A., S. K. Bromley, C. Sumen, M. M. Davis, A. S. Shaw, P. M. Allen, and M. L. Dustin. 1999. The immunological synapse: a molecular machine controlling T cell activation. Science 285: 221–227.
20. Bunnell, S. C., D. I. Hong, J. R. Kardon, T. Yamazaki, C. J. McGlade, V. A. Barr, and L. E. Samelson. 2002. T cell receptor ligation induces the formation of dynamically regulated signaling assemblies. *J. Cell Biol.* 158: 1263–1275.

21. Yokosuka, T., K. Sakata-Sogawa, W. Kobayashi, M. Hiroshima, A. Hashimoto-Tane, M. Tokunaga, M. L. Dustin, and T. Saito. 2005. Newly generated T cell receptor microclusters initiate and sustain T cell activation by recruitment of Zap70 and SLP-76. *Nat. Immunol.* 6: 1253–1262.
22. Seminario, M. C., and S. C. Bunnell. 2008. Signal initiation in T-cell receptor microclusters. *Immunol. Rev.* 221: 90–106.
23. Dustin, M. L. 2009. Supported bilayers at the vanguard of immune cell activation studies. *J. Struct. Biol.* 168: 152–160.
24. Springer, T. A. 1994. Traffic signals for lymphocyte recirculation and leukocyte emigration: the multistep paradigm. *Cell* 76: 301–314.
25. Butcher, E. C. 1991. Leukocyte-endothelial cell recognition: three (or more) steps to specificity and diversity. *Cell* 67: 1033–1036.
26. Choi, J., D. R. Enis, K. P. Koh, S. L. Shiao, and J. S. Pober. 2004. T lymphocyte-endothelial cell interactions. *Annu. Rev. Immunol.* 22: 683–709.
27. Pober, J. S., and W. C. Sessa. 2007. Evolving functions of endothelial cells in inflammation. *Nat. Rev. Immunol.* 7: 803–815.
28. Marelli-Berg, F. M., K. Okkenhaug, and V. Mirenda. 2007. A two-signal model for T cell trafficking. *Trends Immunol.* 28: 267–273.
29. Marelli-Berg, F. M., R. E. Hargreaves, P. Carmichael, A. Dorling, G. Lombardi, and R. I. Lechler. 1996. Major histocompatibility complex class II-expressing endothelial cells induce allospecific nonresponsiveness in naive T cells. *J. Exp. Med.* 183: 1603–1612.
30. Ma, W., and J. S. Pober. 1998. Human endothelial cells effectively costimulate cytokine production by, but not differentiation of, naive CD4+ T cells. *J. Immunol.* 161: 2158–2167.
31. Perez, V. L., L. Henault, and A. H. Lichtman. 1998. Endothelial antigen presentation: stimulation of previously activated but not naïve TCR-transgenic mouse T cells. *Cell. Immunol.* 189: 31–40.
32. Epperson, D. E., and J. S. Pober. 1994. Antigen-presenting function of human endothelial cells. Direct activation of resting CD8 T cells. *J. Immunol.* 153: 5402–5412.
33. Shiao, S. L., N. C. Kirkiles-Smith, B. R. Shepherd, J. M. McNiff, E. J. Carr, and J. S. Pober. 2007. Human effector memory CD4+ T cells directly recognize allogeneic endothelial cells in vitro and in vivo. *J. Immunol.* 179: 4397–4404.
34. Carman, C. V., P. T. Sage, T. E. Sciuto, M. A. de la Fuente, R. S. Geha, H. D. Ochs, H. F. Dvorak, A. M. Dvorak, and T. A. Springer. 2007. Transcellular diapedesis is initiated by invasive podosomes. *Immunity* 26: 784–797.
35. Linder, S. 2009. Invadosomes at a glance. *J. Cell Sci.* 122: 3009–3013.
36. Carman, C. V. 2009. Mechanisms for transcellular diapedesis: probing and pathfinding by 'invadosome-like protrusions'. *J. Cell Sci.* 122: 3025–3035.
37. Carman, C. V., and T. A. Springer. 2004. A transmigratory cup in leukocyte diapedesis both through individual vascular endothelial cells and between them. *J. Cell Biol.* 167: 377–388.
38. Gomez, T. S., S. D. McCarney, E. Carrizosa, C. M. Labno, E. O. Comiskey, J. C. Nolz, P. Zhu, B. D. Freedman, M. R. Clark, D. J. Rawlings, et al. 2006. HS1 functions as an essential actin-regulatory adaptor protein at the immune synapse. *Immunity* 24: 741–752.
39. Sarkar, D., P. K. Vemula, G. S. Teo, D. Spelke, R. Karnik, Y. Wee, and J. M. Karp. 2008. Chemical engineering of mesenchymal stem cells to induce a cell rolling response. *Bioconjug. Chem.* 19: 2105–2109.
40. Antón, I. M., M. A. de la Fuente, T. N. Sims, S. Freeman, N. Ramesh, J. H. Hartwig, M. L. Dustin, and R. S. Geha. 2002. WIP deficiency reveals a differential role for WIP and the actin cytoskeleton in T and B cell activation. *Immunity* 16: 193–204.
41. Wülfing, C., A. Bauch, G. R. Crabtree, and M. M. Davis. 2000. The vav exchange factor is an essential regulator in actin-dependent receptor translocation to the lymphocyte-antigen-presenting cell interface. *Proc. Natl. Acad. Sci. USA* 97: 10150–10155.
42. Billadeau, D. D., J. C. Nolz, and T. S. Gomez. 2007. Regulation of T-cell activation by the cytoskeleton. *Nat. Rev. Immunol.* 7: 131–143.
43. Butler, B., D. H. Kastendieck, and J. A. Cooper. 2008. Differently phosphorylated forms of the cortactin homolog HS1 mediate distinct functions in natural killer cells. *Nat. Immunol.* 9: 887–897.
44. Klos Dehring, D. A., F. Clarke, B. G. Ricart, Y. Huang, T. S. Gomez, E. K. Williamson, D. A. Hammer, D. D. Billadeau, Y. Argon, and J. K. Burkhardt. 2011. Hematopoietic lineage cell-specific protein 1 functions in concert with the Wiskott-Aldrich syndrome protein to promote podosome array organization and chemotaxis in dendritic cells. *J. Immunol.* 186: 4805–4818.
45. Fooksman, D. R., S. Vardhana, G. Vasiliver-Shamis, J. Liese, D. A. Blair, J. Waite, C. Sacristán, G. D. Victora, A. Zanin-Zhorov, and M. L. Dustin. 2010. Functional anatomy of T cell activation and synapse formation. *Annu. Rev. Immunol.* 28: 79–105.
46. Trautmann, A., and S. Valitutti. 2003. The diversity of immunological synapses. *Curr. Opin. Immunol.* 15: 249–254.
47. Bunnell, S. C. 2010. Multiple microclusters: diverse compartments within the immune synapse. *Curr. Top. Microbiol. Immunol.* 340: 123–154.
48. Dovas, A., and D. Cox. 2011. Signaling networks regulating leukocyte podosome dynamics and function. *Cell. Signal.* 23: 1225–1234.
49. Arrieumerlou, C., C. Randriamampita, G. Bismuth, and A. Trautmann. 2000. Rac is involved in early TCR signaling. *J. Immunol.* 165: 3182–3189.
50. Hughes, K., S. Edin, A. Antonsson, and T. Grundström. 2001. Calmodulin-dependent kinase II mediates T cell receptor/CD3- and phorbol ester-induced activation of IkappaB kinase. *J. Biol. Chem.* 276: 36008–36013.
51. Turesson, C. 2004. Endothelial expression of MHC class II molecules in autoimmune disease. *Curr. Pharm. Des.* 10: 129–143.
52. Manes, T. D., S. L. Shiao, T. J. Dengler, and J. S. Pober. 2007. TCR signaling antagonizes rapid IP-10-mediated transendothelial migration of effector memory CD4+ T cells. *J. Immunol.* 178: 3237–3243.
53. Manes, T. D., and J. S. Pober. 2008. Antigen presentation by human microvascular endothelial cells triggers ICAM-1-dependent transendothelial protrusion by, and fractalkine-dependent transendothelial migration of, effector memory CD4+ T cells. *J. Immunol.* 180: 8386–8392.
54. Shulman, Z., V. Shinder, E. Klein, V. Grabovsky, O. Yeger, E. Geron, A. Montresor, M. Bolomini-Vittori, S. W. Feigelson, T. Kirchhausen, et al. 2009. Lymphocyte crawling and transendothelial migration require chemokine triggering of high-affinity LFA-1 integrin. *Immunity* 30: 384–396.
55. Gérard, A., R. A. van der Kammen, H. Janssen, S. I. Ellenbroek, and J. G. Collard. 2009. The Rac activator Tiam1 controls efficient T-cell trafficking and route of transendothelial migration. *Blood* 113: 6138–6147.
56. Sage, P. T., and C. V. Carman. 2009. Settings and mechanisms for trans-cellular diapedesis. *Front. Biosci.* 14: 5066–5083.
57. Albiges-Rizo, C., O. Destaing, B. Fourcade, E. Planus, and M. R. Block. 2009. Actin machinery and mechanosensitivity in invadopodia, podosomes and focal adhesions. *J. Cell Sci.* 122: 3037–3049.
58. Bunnell, S. C., A. L. Singer, D. I. Hong, B. H. Jacque, M. S. Jordan, M. C. Seminario, V. A. Barr, G. A. Koretzky, and L. E. Samelson. 2006. Persistence of cooperatively stabilized signaling clusters drives T-cell activation. *Mol. Cell. Biol.* 26: 7155–7166.
59. Wetzel, S. A., T. W. McKeithan, and D. C. Parker. 2002. Live-cell dynamics and the role of costimulation in immunological synapse formation. *J. Immunol.* 169: 6092–6101.
60. Barcia, C., A. Gomez, V. de Pablos, E. Fernández-Villalba, C. Liu, K. M. Kroeger, J. Martín, A. F. Barreiro, M. G. Castro, P. R. Lowenstein, and M. T. Herrero. 2008. CD20, CD3, and CD40 ligand microclusters segregate three-dimensionally in vivo at B-cell-T-cell immunological synapses after viral immunity in primate brain. *J. Virol.* 82: 9978–9993.
61. Barcia, C., N. S. Sanderson, R. J. Barrett, K. Wawrowsky, K. M. Kroeger, M. Puntel, C. Liu, M. G. Castro, and P. R. Lowenstein. 2008. T cells' immunological synapses induce polarization of brain astrocytes in vivo and in vitro: a novel astrocyte response mechanism to cellular injury. *PLoS ONE* 3: e2977.
62. Barcia, C., Jr., A. Gómez, J. M. Gallego-Sanchez, A. Perez-Vallés, M. G. Castro, P. R. Lowenstein, C. Barcia, Sr., and M. T. Herrero. 2009. Infiltrating CTLs in human glioblastoma establish immunological synapses with tumorigenic cells. *Am. J. Pathol.* 175: 786–798.
63. Davis, D. M. 2009. Mechanisms and functions for the duration of intercellular contacts made by lymphocytes. *Nat. Rev. Immunol.* 9: 543–555.
64. Rudd, P. M., T. Elliott, P. Cresswell, I. A. Wilson, and R. A. Dwek. 2001. Glycosylation and the immune system. *Science* 291: 2370–2376.
65. Valitutti, S., M. Dessing, K. Aktories, H. Gallati, and A. Lanzavecchia. 1995. Sustained signaling leading to T cell activation results from prolonged T cell receptor occupancy. Role of T cell actin cytoskeleton. *J. Exp. Med.* 181: 577–584.
66. Negulescu, P. A., T. B. Krasieva, A. Khan, H. H. Kerschbaum, and M. D. Cahalan. 1996. Polarity of T cell shape, motility, and sensitivity to antigen. *Immunity* 4: 421–430.
67. Wei, X., B. J. Tromberg, and M. D. Cahalan. 1999. Mapping the sensitivity of T cells with an optical trap: polarity and minimal number of receptors for Ca(2+) signaling. *Proc. Natl. Acad. Sci. USA* 96: 8471–8476.
68. Ma, Z., K. A. Sharp, P. A. Janmey, and T. H. Finkel. 2008. Surface-anchored monomeric agonist pMHCs alone trigger TCR with high sensitivity. *PLoS Biol.* 6: e43.
69. Ma, Z., P. A. Janmey, and T. H. Finkel. 2008. The receptor deformation model of TCR triggering. *FASEB J.* 22: 1002–1008.
70. Groves, J. T. 2007. Bending mechanics and molecular organization in biological membranes. *Annu. Rev. Phys. Chem.* 58: 697–717.
71. Xu, C., E. Gagnon, M. E. Call, J. R. Schnell, C. D. Schwieters, C. V. Carman, J. J. Chou, and K. W. Wucherpfennig. 2008. Regulation of T cell receptor activation by dynamic membrane binding of the CD3epsilon cytoplasmic tyrosine-based motif. *Cell* 135: 702–713.
72. Dustin, M. L., S. Y. Tseng, R. Varma, and G. Campi. 2006. T cell-dendritic cell immunological synapses. *Curr. Opin. Immunol.* 18: 512–516.
73. Saito, T., and T. Yokosuka. 2006. Immunological synapse and microclusters: the site for recognition and activation of T cells. *Curr. Opin. Immunol.* 18: 305–313.
74. Burbach, B. J., R. B. Medeiros, K. L. Mueller, and Y. Shimizu. 2007. T-cell receptor signaling to integrins. *Immunol. Rev.* 218: 65–81.
75. Perez-Moreno, M., C. Jamora, and E. Fuchs. 2003. Sticky business: orchestrating cellular signals at adherens junctions. *Cell* 112: 535–548.
76. Harwood, N. E., and F. D. Batista. 2008. New insights into the early molecular events underlying B cell activation. *Immunity* 28: 609–619.
77. Vicente-Manzanares, M., and F. Sánchez-Madrid. 2004. Role of the cytoskeleton during leukocyte responses. *Nat. Rev. Immunol.* 4: 110–122.
78. Miranti, C. K., and J. S. Brugge. 2002. Sensing the environment: a historical perspective on integrin signal transduction. *Nat. Cell Biol.* 4: E83–E90.
79. Luxenburg, C., D. Geblinger, E. Klein, K. Anderson, D. Hanein, B. Geiger, and L. Addadi. 2007. The architecture of the adhesive apparatus of cultured osteoclasts: from podosome formation to sealing zone assembly. *PLoS ONE* 2: e179.
80. Destaing, O., A. Sanjay, C. Itzstein, W. C. Horne, D. Toomre, P. De Camilli, and R. Baron. 2008. The tyrosine kinase activity of c-Src regulates actin dynamics and organization of podosomes in osteoclasts. *Mol. Biol. Cell* 19: 394–404.
81. Saltel, F., O. Destaing, F. Bard, D. Eichert, and P. Jurdic. 2004. Apatite-mediated actin dynamics in resorbing osteoclasts. *Mol. Biol. Cell* 15: 5231–5241.

SUPPLEMENTAL FIGURE & VIDEO LEGENDS

Fig. S1. Phenotype and Activation of Memory-like CD4 T cells to Endothelial Presented Ag

(A) CD4 nT_{mem} cells were sorted from human blood according to *Materials and Methods*, stained for indicated surface markers and analyzed by flow cytometry.

(B) Surface phenotype of cultured induced T memory cells (iT_{mem}). CD4 T cells were isolated, activated and cultured according to *Experimental Procedures*, stained for indicated surface markers and analyzed by flow cytometry. Plots are only CD4 positive gate.

(C). HLMVEC were incubated with or without IFN-γ for 48 hours and with or without TNF-α for 18 hours, trypsinized, stained for MHC II, and analyzed by flow cytometry.

(D) TSST/SEB- or MAM-selective iT_{mem} were generated in parallel by initial T cell expansion in the presence either TSST/SEB or the atypical super-antigen MAM. HLMVEC were activated with TNF-α, -/+INF-γ and pulsed -/+ MAM and then incubated for 30 min with either 'TSST/SEB-iT_{mem}' or 'MAM-iT_{mem}' and percent transmigrated cells scored. Note that MAM-iT_{mem}', but not 'TSST/SEB-iT_{mem}' exhibited significantly retarded transendothelial migration on MAM pulsed endothelium, demonstrating selectivity in model Ag responsiveness.

(E) IT_{mem} were added the upper chamber or transwell dishes containing activated/Ag-pulsed HLVMELs. After a 6 hour incubation the transmigrated lymphocytes that entered the lower chamber were collected stained for CD62L and CD69 and analyzed by flow cytometry. IT_{mem} treated directly with PMA and Ionomycin ('PMA/IONO') were used as positive activation control.

(F) Samples were prepared as in (E) with the addition of golgistop in the lower chamber for the last 3 hours of incubation. Cells were permeabilized, stained for IFN-γ and subject to flow cytometry.

(G) Quantitation of Samples in (F). Error bars indicate standard error.

(H) Samples were prepared as in (E) with CFSE pre-labeling of iT_{mem} and 72 hour incubation in transwells before collection and flow cytometric analysis.

Fig. S2. Morphology and Dynamics of Ag-Stabilized ILPs

(A) Samples were prepared under shear flow as in Fig. 1E and then fixed by perfusion post T cell infusion. Samples were stained for LFA-1 (red) and ICAM-1 (green) and imaged by confocal microscopy.

(B) Live cell imaging of nT_{mem} interacting with activated, Ag-pulse HLMVECs was conducted as in Fig. 2B. Arrays of stabilized podo-prints (arrows) were readily seen to form on the mem-DsRed expressing EC surface. Additionally, ratiometric calcium imaging was conducted with these Fura-2-labeled nT_{mem} cells (lower panels).

(C) Calcium flux (red line) is plotted over time for individual cell depicted in (B). Black vertical lines indicate the time points when initial ILPs and stable ILP arrays were formed.

(D). Samples were prepared as in Fig. S1D on mem-YFP-transfected HLMVECs (green) pulsed with alternate model bacterial super-Ag MAM and fixed after 5 min co-incubation. Samples were then stained for CD3 (red) and F-actin (blue) and imaged by confocal microscopy.

(E) Previously activated murine OT-II CD4 T cells were Fura-2-loaded and incubated on IFN-γ, OVA 323-339 pulsed cardiac microvascular ECs.

Fig. S3 Distribution of Immune Signaling Molecules in the T cell-EC IS

IT_{mem} cells were incubated with activated, Ag-pulsed (TSST/SEB) (and ICAM-1-GFP or mem-YFP-transfected, where indicated) HLMVEC for 5 (A, B, D) or 30 min (C), fixed, and stained as indicated and imaged by confocal microscopy.

(A) Samples on mem-YFP (green)-transfected ECs were stained for MHC-II (red). Representative micrograph is shown on the left. Middle panel indicates fluorescent values of each channel from line scan (dashed line on left). Right indicates quantitation of fluorescence intensities along the dashed line comparing podo-prints from nearby regions of endothelium outside of the T cell contact zone.

(B) Samples were prepared as in (A) on ICAM-1-GFP or mem-YFP-expressing HLMVECs and stained for CD3, CD43 or CD45 and LFA-1 as indicated. *En face* (x-y) and orthogonal cross-sectional (x-z, y-z) views are depicted. CD3, CD43 and CD45 are pseudo-colored using a rainbow intensity indicator (blue = low, red = high). Left panels show a relatively basal section (see yellow arrows) at the T cell-EC interface where the podo-print- and ILP arrays are evident (red arrows). Right panel shows a section that is relatively more apical (i.e., distal from the IS, see orange arrows). Note that CD3 has highest intensity within the ILPs compared to parallel oriented segments at the edge of the cell in regions outside of the IS (i.e., the D-SMAC). By contrast, CD43 and CD45 intensity is highest outside of the IS (i.e., in the D-SMAC), shows modest levels within the peripheral ILP region and is lowest in the center if the IS.

(C) Samples were stained for F-actin (blue), LFA-1 (green) and CD3 (red). Whereas, on the majority of T cells CD3 was either enriched into ILPs after 30 min (upper panels), only a very small fraction (<5%) of cells displayed enriched into cSMAC-like central clusters. A similar fraction showed relatively more diffuse distributions (data not shown).

(D) Samples were stained for F-actin (green and rainbow intensity pseudo-color) and PKC-Θ (red and rainbow intensity pseudo-color), subjected to confocal microscopy and presented as *en face* and orthogonal projections.

Scale bars represent 5 μm.

Fig. S4. Characterization of Planar Coated-Glass/-Cell IS Models and the T cell-B Cell IS

(A) IT_{mem} were loaded with Fluo-4 and added to imaging chambers coated with ICAM-1-Fc and either anti-CD43, -45 or CD3 (OKT3) antibodies. Cells were imaged after 5 min incubation on each substrate and fluorescence intensity of Fluo-4 in each of at least 50 cells from two separate experiments was measured and background (mean fluorescence of Fluo-4 loaded onto uncoated/HSA-blocked chambers) subtracted. Values represent mean ± S.E.M.

(B) iT_{mem} samples as in (A) were imaged during initial interactions. Arrows indicate IRM-detected 'micro-contacts'.

(C) Offset time calculated from experiments as in (B).

(D and E) Imaging as in (B) on chambers coated with ICAM-1-Fc and either anti-CD45 (D) or -CD3 (E). Arrows indicated micro-contacts formed under spreading lamellipodia. See also Video 9.

(F) CHO-K1 cells were incubated with or without (specificity control) primary amine cell surface biotinylation agent, followed by binding of streptavidin and capture of anti-CD3 antibody OKT3. To validate this procedure we monitored cell surface capture of fluorescent streptavidin (not shown) and capture of antibody by staining with fluorescent secondary antibody goat anti-mouse (GAM)-Cy3.

(G) Offset time calculated from experiments as in (Fig. 8D).

(H) Left panel shows a schematic of typical lateral interactions formed between T cell and B cells *in vitro*, in which the IS is oriented along the z-axis. Insets 1 and 2 show schematic cross-sections from the edge and equator of the IS, respectively. Right panels show confocal cross sections of iT_{mem} interacting with Ag-pulsed Priess B cells for 5 min and stained for LFA-1. Equatorial cross-section (panel 2a) revealed peripheral lymphocyte buldges enriched in LFA-1 (arrows). Edge cross-sections (panels 1a-d) reveal finger-like LFA-1-enriched projections (arrows).

Scale bars represent 5 μm.

Video 1. IT_{mem} CD4 T Cells Transiently Arrest Migration Under Shear Flow in Response to Ag.

Video depicts iT_{mem} CD4 T cells interacting with IFN-γ/TNF-α-activated HLMVEC under 2 dyne/cm^2 laminar fluid shear flow in the absence (‘Control’, left) and presence (‘+Ag’; right) of pulsed TSST/SEB and corresponds to Fig. 1E. Cells were infused at 1 million/ml for 30 seconds. Video is 10 frames per second. Scale bar represents 50 μm.

Video 2. IT_{mem} CD4 T Cells Probe the Endothelium with Dynamic ILPs

Video depicts an iT_{mem} CD4 T cell 'probing' IFN-γ/TNF-α-activated and mem-YFP transfected HLMVEC with dynamic ILPs and corresponds to Fig. 2A. Upper panels show DIC and lower panels show mem-YFP. Individual fluorescent rings (i.e., podo-prints) form and disappear continuously as lymphocytes laterally migrate over the endothelium reflecting dynamic probing by rapid insertion and retraction of T cell ILPs. Video is 5 frames per second. Scale bar represents 5 μm.

Video 3. IT_{mem} ILPs Become Stabilized and Form Dense Peripheral Arrays on Ag Presenting Endothelium

Video depicts an iT_{mem} CD4 T cell interacting with IFN-γ/TNF-α-activated, Ag-pulsed and mem-YFP transfected HLMVEC and corresponds to Fig. 2B 'Ag Example 1'. Upper panels show DIC and lower panels show mem-YFP. As seen by DIC two lymphocytes exhibit different degrees of spreading without significant polarization or lateral migration. At the same time several initial podo-prints are seen to form on the endothelium that rapidly transition to dense arrays of ILPs predominantly localized to the peripheral/lamellipodial zone of the T cell-EC contact. Once formed most individual ILPs persist throughout the duration of the video (15 min) during which time they exhibit limited shape change and lateral translocation. Toward the end of the video some podo-prints shrink and/or disappear, suggesting retraction of ILPs. Other ILPs apparently begin to drive formation of trans-cellular pores in the endothelium as noted by the black spots that appear where podo-prints were formerly located. Video is 5 frames per second. Scale bar represents 5 μm.

Video 4. A Minority of IT_{mem} Form Rosette Type Arrays of Stabilized ILPs on Ag Presenting Endothelium

Video depicts an iT_{mem} CD4 T cell interacting with IFN-γ/TNF-α-activated, Ag-pulsed and mem-YFP transfected HLMVEC and corresponds to Fig. 2B 'Ag Example 2'. Upper panels show DIC and lower panels show mem-DsRed. As seen by DIC a lymphocyte spreads a symmetrical ruffle without lateral migration. As seen on EC mem-DsRed, several initial podo-prints are seen to form on the endothelium that rapidly transition to a dense peripheral array localized to the T cell lamellipodial zone. Subsequent addition of more central podo-prints then leads to rosette type clusters by ~10 min. Once formed most individual ILPs persist throughout the duration of the video (45 min) during which time they exhibit limited shape change and lateral translocation. Toward the end of the video some podo-prints shrink and/or disappear, suggesting retraction of ILPs. Other ILPs apparently begin to drive formation of trans-cellular pores in the endothelium as noted by the black spots that appear where podo-prints were formerly located. Video is 5 frames per second. Scale bar represents 5 μm.

Video 5. Ag Stabilized ILPs are Enriched in Integrin LFA-1 and Podo-prints Enriched in ICAM-1

Video depicts 3D rotation of ILP arrays formed by iT_{mem} bound for 5 min to activated HUVEC, pulsed with Ag (SEE) and corresponds to Fig. 3B. Samples were stained for ICAM-1 (green) and LFA-1 (red) and subjected to serial-section (0.3 μm thickness) confocal imaging followed by digital reconstruction. To enhance the visualization of the ILP architecture, as a series of 30 three-dimensional projections were rendered, each

representing successive rotation about both the x and z axis in 3° intervals for a total of 90° about each axis, and played in series. Note that individual ILPs can clearly be seen to form LFA-1-enriched three-dimensional, cylindrically-shaped, micron-scale protrusions, whereas podo-prints are clearly the cognate 3D ICAM-1-enriched endothelial invaginations into which the ILPs extend.

Video 6. Ag-Stabilized ILP Arrays are Highly Enriched in HS1

Video depicts 3D rotation of HS1 (red) enriched ILP arrays formed by iT_{mem} bound to activated, Ag-pulsed HLMVECs for 5 min and corresponds to Fig. 4H. Samples were subjected to serial-section (0.3 μm z-step) confocal imaging. Images were digitally reconstructed and rendered as a series of 3D-projections with progressive rotations about the x, y and z axes to enhance the visualization of architectural details. Note that HS1 is highly enriched into three-dimensional, cylindrically-shaped, micron-scale lymphocyte projections arranged as dense arrays at the periphery of the T cell-EC contact area.

Video 7. ILPs Precede and are Stabilized by Ag-Dependent Calcium Flux

Video depicts Fura-2-labeled iT_{mem} CD4 interacting with mem-DsRed-transfected, activated and Ag-pulsed HLMVECs and corresponds to Fig. 5A. Note that a single central podo-print/ILP initially forms (time stamp = 00:00 min:sec) and precedes initiation of calcium flux by 20 seconds (offset time = 20 sec). By approximately 1 min after initial podo-print/ILP peak calcium flux is established commensurate with transition to peripheral arrays of stabilized podo-prints/ILPs. These arrays persist over the

duration of the video, but individual ILPs become less well-defined (and in this particular example undergo limited centripetal translocation as calcium signal begins to decay. Video is 5 frames per second. Scale bar represents 2 μm.

Video 8. OT-I CTL T Cells Probe the Endothelium with Dynamic ILPs

Video depicts an OT-I CTL 'probing' IFN-γ/TNF-α-activated and mem-YFP transfected murine heart MVEC with dynamic ILPs and corresponds to Fig. 7C. A. Left panel show DIC, right panel show mem-YFP. Note that the CTL avidly probes the endothelial surface by constant formation and retraction of clusters of ILPs (evidenced by micron-scale fluorescent rings, i.e., podo-prints) under the leading edge lamellipodia. Here in the absence of cognate Ag, lateral migration and rapid ILP turnover (~20 sec lifetime) persist. Video is 5 frames per second. Scale bar represents 5 μm.

Video 9. Dynamics of Initial and Peripheral Arrays of T cell 'Micro-Contacts' during Interaction with Anti-CD3-Coated Glass.

Video depicts 3 sequential examples of iT_{mem} CD4 T cells interacting with ICAM-1-/anti-CD3-coated glass. Example #1 corresponds to Fig. S4E. Note that in each example cells initially form a few IRM-resolved micro-contacts (i.e., dark spots), followed by rapid spreading of symmetrical lamellipodia under which arrays of micro-contacts continue to form. Video is 10 frames per second. Scale bar represents 5 μm.

Video 10. T cells form 3D ILPs on anti-CD3-'Coated' CHO-K1 Cells.

Video depicts Fura-2 labeled iT_{mem} cells interacting with a planar cell-coated APC model and corresponds to Fig. 8D. CHO-K1 cells were transfected to express cell-surface ICAM-1-GFP (green) and intracellular soluble DsRed (red) and then with 'coated' anti-CD3 antibody using a cell surface biotinylation/streptavidin capture approach. Note the clear appearance of ICAM-1-GFP fluorescent rings and correlating circular regions of displaced sDsRed indicating CHO-K1 cell surface invagination that precede initial calcium flux by several frames (i.e., offset time 56 $\pm$ 17 sec). Arrays of clustered, rosette-type arrays form commensurate with increased calcium flux. Video is 10 frames per second. Scale bar represents 5 μm.

Video 11. IT_{mem} Cells Form ILPs during Initial Interaction with Ag-Pulsed Priess B Cells. Priess B cells were allowed to adhere to coverglass coated with anti-CD20 and then pulsed with antigen as described in *Experimental Procedures.* IT_{mem} cells were added to the wells and incubated for 5 min before samples were fixed and stained for F-actin (green) and LFA-1 (red). Confocal images were acquired and 3D digital reconstructions rendered. Movie represents one such reconstruction (corresponding to Fig. 8G) where the T cell (white outline) settled on top of the B cell (blue dashed line) fortuitously forming quasi *en face* IS (red overlay), which is rotated about the z-axis over time. Peripheral lymphocyte ILPs rich in LFA-1 and F-actin are clearly evident T cell-B cell contact zone.

Sage Figure S1

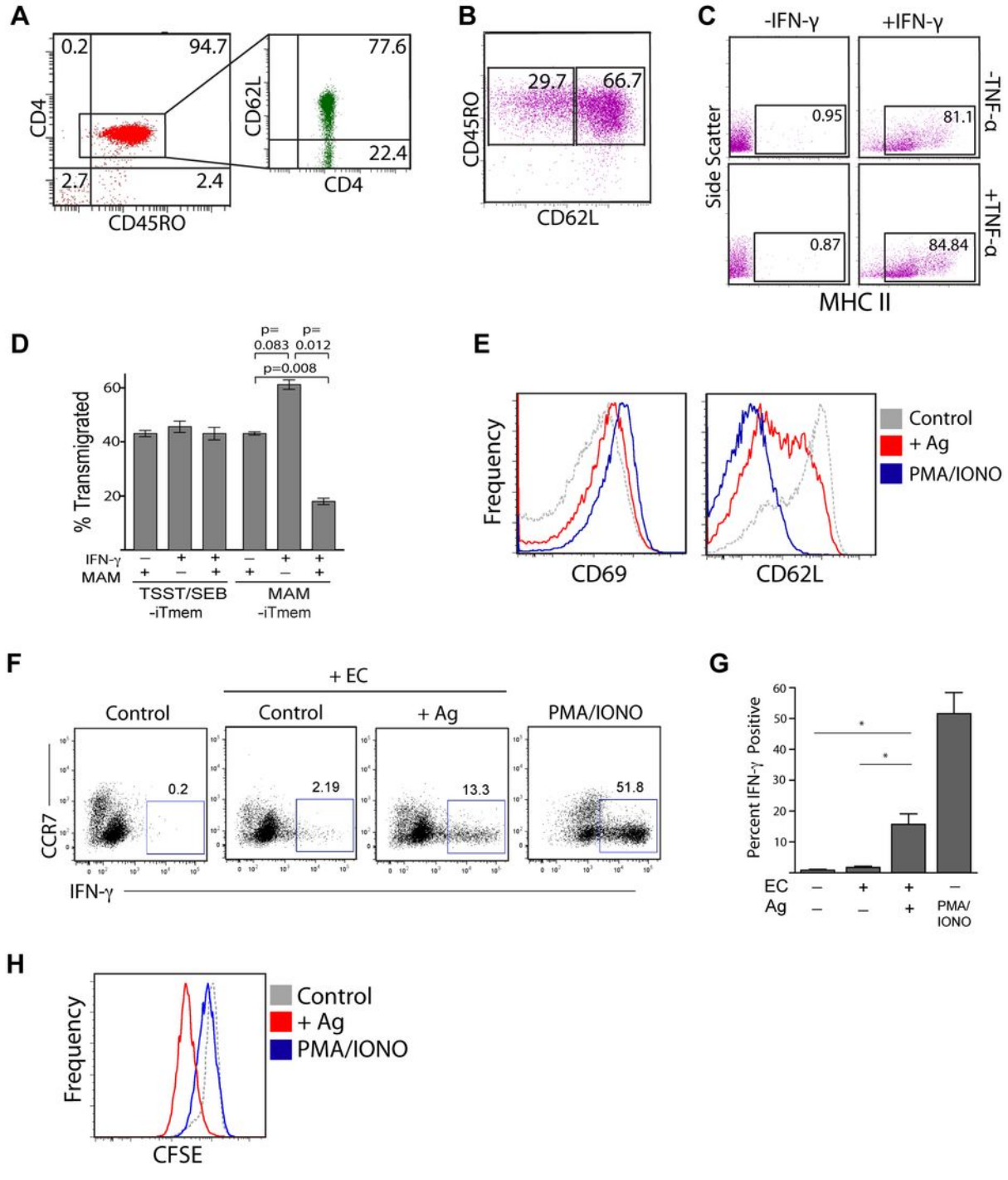

Sage Figure S2

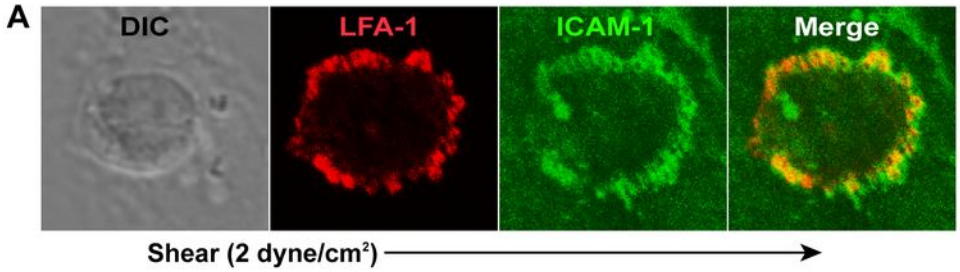

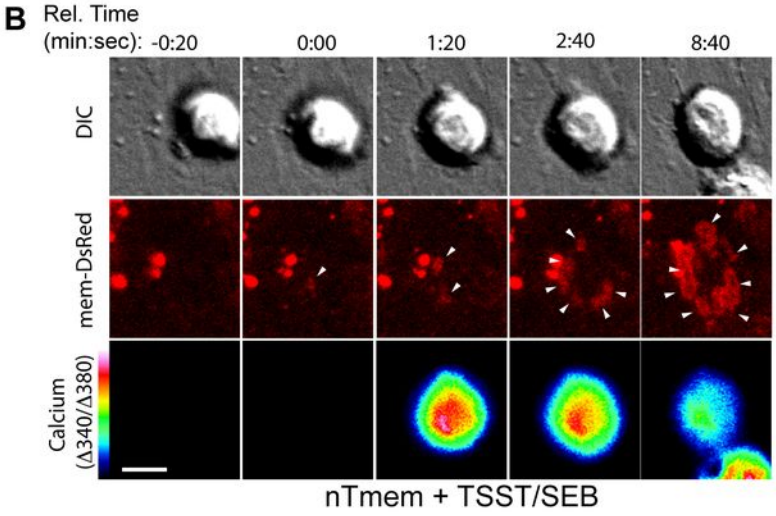

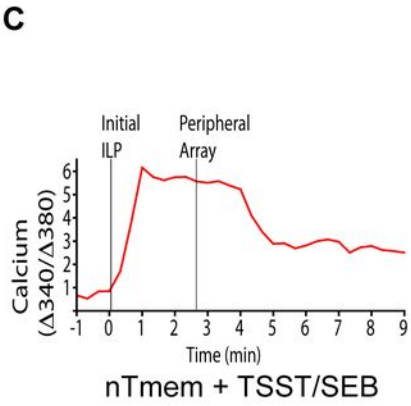

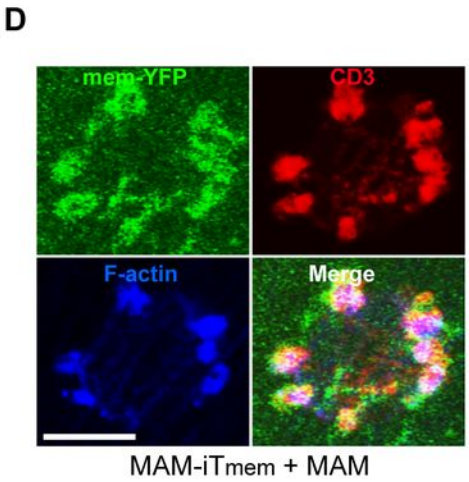

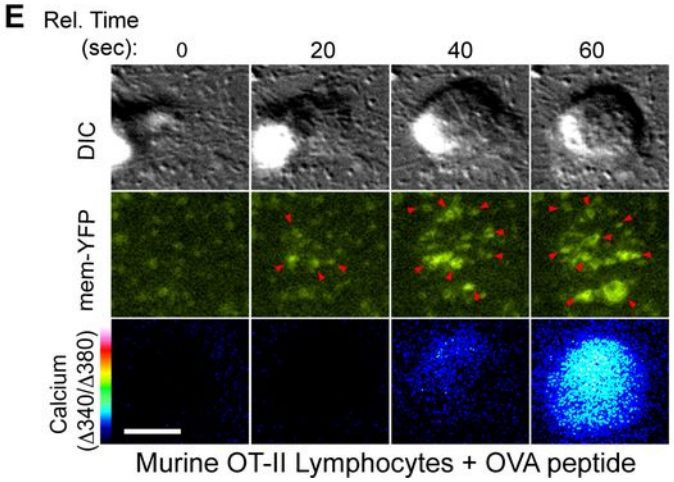

Sage Figure S3

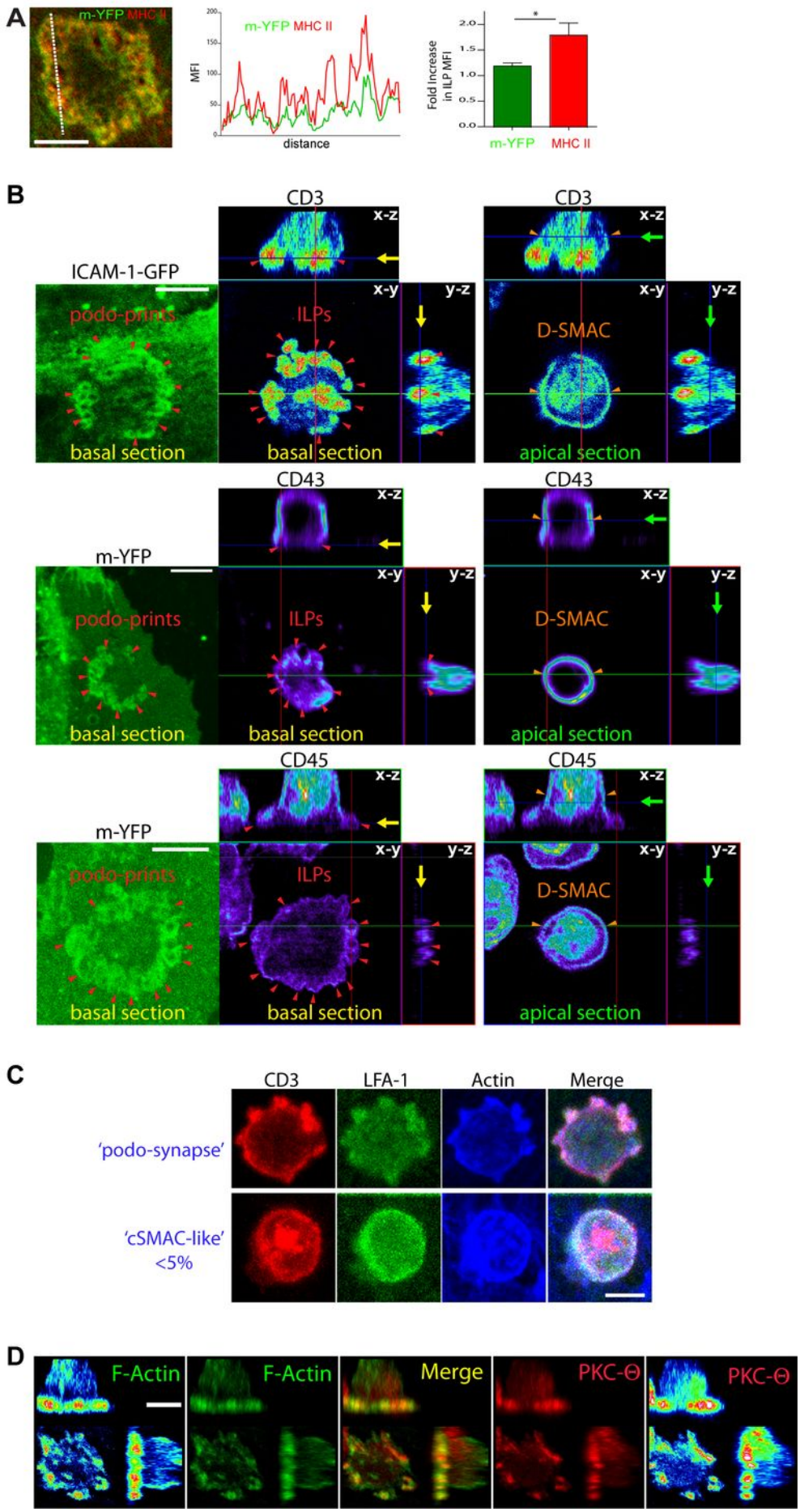

Sage Figure S4